https://doi.org/10.5194/egusphere-2025-400
Preprint. Discussion started: 19 February 2025


# High-Resolution Paleo-Storm Reconstruction from Eastern Canada Aligns with Late-Holocene Northwestern Atlantic Hurricane Records

Antoine Lachance[1], Matthew Peros[2,3], Jeannine-Marie St-Jacques[1,3], Pierre Francus[4,3], Nicole K. Sanderson[5,3]

[1] Department of Geography, Environment and Planning, Concordia University, Montreal, H3G 1M8, Canada
[2] Department of Environmental, Agriculture, and Geography, Bishops University, Sherbrooke, J1M 1Z7, Canada
[3] GEOTOP – Research Center in Earth System Dynamics, Montreal, H3C 3P8, Canada
[4] INRS – Institut National de la Recherche Scientifique, Centre Eau, Terre, Environnement, Québec, G1K 9A9, Canada
[5] Département de Géographie, UQAM – Université du Québec à Montréal, Montreal, H2X 3R9, Canada

*Correspondence to*: Antoine Lachance (antoine.lachance@mail.concordia.ca)

**Abstract**

Atlantic Canada experiences frequent major storms, particularly tropical cyclones transitioning into post-tropical storms. Events such as Hurricane Fiona (2022), Dorian (2019), and Juan (2003) have caused significant damage, loss of life, and coastal erosion, exacerbated by sea level rise and warming waters. Despite this, centennial- to millennial-scale storm records in the region remain scarce. Existing studies in North America focus primarily on marine and coastal overwash records, with limited use of aeolian mineral inputs in ombrotrophic peatlands as storm proxies. Here, we address these gaps by analysing grain-size and geochemical data from two peatlands in Quebec, Canada's Magdalen Islands.

Our two peat records reveal consistent storm signals over the past 4000 years, with three key periods of heightened activity: 800–550 BCE, 600–800 BCE, and 1300–1700 CE. These signals align with marine and overwash records spanning the past 2000 years across eastern Canada, the US, and the Bahamas, indicating low storm activity during the Medieval Climate Anomaly, followed by increased activity during the Little Ice Age. Our findings suggest that storm records in these regions are influenced by local climatic factors. Negative phases of the Atlantic Multidecadal Variability, which typically suppress hurricane activity in the North Atlantic, are associated with conducive hurricane formation and intensification north of the Bahamas. Additionally, the position of the Bermuda High seems to play a more significant role in directing storm tracks during different climatic phases. Our findings highlight the potential antiphase relationship in storm activity between regions north of the Bahamas and those in the Gulf of Mexico, suggesting broader climatic mechanisms that warrant further investigations.

Despite the similarities between our two sites, discrepancies in geochemistry and mineralogical profiles highlight the importance of site-specific conditions in interpreting the storm record from peatlands, namely the distance of the sites to the coast and source of aeolian sediment, as well as peatland size. Challenges also remain in calibrating peat-based proxies with historical storm records, as identifying specific events from the past 150 years remains difficult.

https://doi.org/10.5194/egusphere-2025-400
Preprint. Discussion started: 19 February 2025


## 1 Introduction

Atlantic Canada is frequently impacted by major storms, which have resulted in considerable damage and occasional death, especially from storms of tropical origins that have transitioned into powerful post-tropical cyclones (Baker et al., 2021; Public Safety Canada, 2024). Most recently, in September 2022, Hurricane Fiona made landfall in Nova Scotia with winds as strong as a category 2 event before tracking northwards through the Gulf of St. Lawrence and striking southwestern Newfoundland, becoming the costliest extreme event in Atlantic Canada ever (Insurance Bureau of Canada, 2022; Pasch et al., 2023). In September 2019, Hurricane Dorian passed over central Nova Scotia, eastern Prince Edward Island, and the Magdalen Islands, and resulted in large-scale wind-induced damage to trees and infrastructure and severe storm surges up to 5 feet above normal levels (Avila et al., 2020). In September 2003, Hurricane Juan made landfall east of Halifax, Nova Scotia, as a category 1 event, causing eight deaths (Avila, 2003). Such events, coupled with ongoing sea level rise, are also contributing to coastal erosion in areas of the Gulf of St. Lawrence such as the Magdalen Islands and Prince Edward Island, while the waters surrounding these islands are warming at a rate faster than almost any other region in the world (Barnett et al., 2017; Rémillard et al., 2017; Barnett et al., 2019; Wu et al., 2022). Consequently, how the frequency and intensity of high magnitude storm events will change in the future are important questions to consider, especially given record-setting sea surface temperatures in the North Atlantic during the past several years (Lapointe et al., 2020).

Answering these questions is aided by a long-term perspective, but there has been very little research examining centennial- to millennial-scale storm records in Atlantic Canada. One exception is a study from Robinson Lake, Nova Scotia, which used sediment grain-size and geochemistry to infer a period of enhanced impacts interpreted as being caused by storms of tropical origins during the Little Ice Age (LIA) (Oliva et al., 2017), the results of which are comparable to similar studies from New England (Van De Plassche et al., 2006; Besonen et al., 2008; Boldt et al., 2010; Donnelly et al., 2015). In New Brunswick, an inland lake record revealed a high concentration of storm impacts during the early LIA (before *ca*. 1650 CE) and from 1895 CE to the present (Patterson et al., 2022). Moreover, evidence for a powerful (possibly category 4) post-tropical cyclone strike on Cape Breton Island, Nova Scotia, was also found to have occurred during the period from 1756–1763 (Dickie and Wach, 2024). In southern Newfoundland, sedimentary records from several coastal lagoons have been used to infer a series of marine flood events occurring over the last several hundred years, which were attributed to both storms and tsunamis (Pleskot et al., 2023). Finally, a 6.5 ka record of storms was developed from a marine core collected from the Scotian Shelf, offshore Nova Scotia, using sand content and elemental ratios such as Zr/Fe and Zr/Ti (Yang et al., 2020). The results show that storm frequency was sometimes synchronized between low and middle latitudes, particularly during 4.5–2.5 ka and since 0.5 ka, while at other times it was asynchronous.

Throughout the western North Atlantic, paleo-storm reconstructions have largely relied on marine overwash signals in nearshore or littoral sedimentary basins, which have provided considerable insights into late Holocene storm dynamics and driving mechanisms (Liu and Fearn, 1993, 2000; Lane et al., 2011; Braun et al., 2017; Bregy et al., 2018; Oliva et al., 2018; Wallace et al., 2021b; Wang et al., 2024). At many locations in the Bahamian Archipelago, coastal karst basins, including blue

https://doi.org/10.5194/egusphere-2025-400
Preprint. Discussion started: 19 February 2025


holes, have been increasingly used to provide high-resolution, decadal to centennial sedimentary records of intense tropical cyclone strikes. These records have revealed periods of enhanced activity, particularly during the Little Ice Age (Van Hengstum et al., 2014; Wallace et al., 2019; Wallace et al., 2021b; Winkler et al., 2023). Similarly, in the Gulf of Mexico, sedimentary records from lagoons, coastal lakes, and karst basins across western Florida, Texas, and Belize have provided comparable high-resolution, decadal to centennial data. However, these records indicate a reduction in tropical cyclone activity during the Little Ice Age (Lane et al., 2011; Brandon et al., 2013; Denommee et al., 2014; Rodysill et al., 2020; Monica et al., 2024; Wang et al., 2024). As records of marine incursions, such studies provide information largely about storm surges, and the degree to which these correlate with storm size is unclear (Irish et al., 2008). Moreover, marine incursions can also occasionally be confused with tsunami strikes, although such events are relatively rare in eastern North America (Ten Brink et al., 2014).

In contrast, paleo-storm studies in the European context have often focused on the use of allochthonous mineral input into ombrotrophic coastal peatlands located nearby beaches or dunes (Björckl and Clemmensen, 2004; Goslin et al., 2019; Vandel et al., 2019; Kylander et al., 2020; Sjöström et al., 2024). The premise is that storm events transport fine sand to such peatlands, whose mineral input is predominately dependent on atmospheric input (Shotyk, 1988; Weiss et al., 2002). Such data, measured using grain-size and geochemical indicators, provide a record of aeolian sediment influx, and ultimately storm-wind activity, which has been argued to reflect "storminess" — the frequency and intensity of storms over a given period (Björckl and Clemmensen, 2004; Vandel et al., 2019). For example, a recent study from Sweden used mid-infrared (MIR) spectral data from a large coastal ombrotrophic bog and showed a series of six periods of enhanced activity over the last 5000 years (Kylander et al., 2023). Moreover, at a site in Denmark, mineral grain size was used to infer wind intensity, which was seen to be high during negative NAO phases (Goslin et al., 2019). In addition to yielding information on wind characteristics, peatlands also often have long-term morphometric stability, limited bioturbation, and abundant macrofossils for radiometric dating, facilitating the interpretation of such records. A critical question remains whether aeolian paleo-storm reconstructions can be directly compared with marine and overwash-based paleo-storm records from nearby coastal sites.

We are unaware of any published research on paleo-storms in eastern North America using aeolian mineral input into ombrotrophic peatlands. The purpose of our paper is thus threefold: 1) to add new, long-term data on the frequency of storm events from an understudied region, namely Atlantic Canada; 2) to develop the first wind-based paleo-storm reconstructions from North American peatlands; and 3) to explore whether findings from these reconstructions align with marine records from the nearby region, the North American eastern seaboard. We focus on two previously unstudied ombrotrophic peatlands located on the Magdalen Islands, Quebec, Canada. Our detection of storms is based on a combination of sediment grain-size and high-resolution micro-XRF core scanning elemental data from both sites.

https://doi.org/10.5194/egusphere-2025-400
Preprint. Discussion started: 19 February 2025


## 2 Context

### 2.1 Location of study

Located in the Gulf of the St. Lawrence (GSL) (Fig. 1), the Magdalen Islands (47°26'54"N, 61°45'08"W) are an archipelago consisting of basaltic hills surrounded by karstic foothills and sandstone platforms (Hétu et al., 2020), with the sandstone primarily composed of quartz and being the main sand source for the island's beaches (Adomat and Gischler, 2017). These hills are connected by a system of barrier beaches, tombolos, and lagoons that formed for the most part after 600 BCE (Rémillard et al., 2015; Barnett et al., 2017). The Magdalen Islands' climate is strongly maritime, with cool summers, mild winters, and steady winds from all directions (Hétu et al., 2020). Daily maximum temperature is highest in July, reaching 21°C for the period 1981–2010, and is lowest in February at 4.3°C for the same period (Environment and Climate Change Canada, 2024). Monthly precipitation is relatively stable throughout the year, although is highest in November at 109 mm and lowest in late winter (February, March, April) and July at around 75 mm (Environment and Climate Change Canada, 2024). The wind direction shows a distinct seasonality, with winds from the south southwest in spring and summer (40–50 km/hr for 15% of the time), and from the northwest in the fall and winter, which are occasionally much stronger (70–132 km/hr for 15% of the time) (Appendix A, Fig. A1). Sea ice cover in the Gulf of St. Lawrence normally begins in December and extends until April each winter (Canadian Ice Service, 2022), although over the past two decades sea ice around the Magdalen Islands has been diminishing (Derksen et al., 2019).

Previous work on the Late Quaternary history of the Magdalen Islands has provided insights into the pre- and post-glacial coastal environments of the area (Prest et al., 1976; Dredge et al., 1992). The Magdalen Islands were deglaciated by approximately 20 ka and were largely submerged by marine water until about 15 ka. Following this, glacial-isostatic rebound resulted in the emergence of the islands and relative sea level (RSL) fell, resulting in a low-stand at 9–10 ka (Rémillard et al., 2016). Next, due to eustatic processes, submergence occurred, so that by 6 ka RSL was approximately 20 m below present level, and then rose at a decelerating rate to its present position (Vacchi et al., 2018; Barnett et al., 2019). At Havre-Aubert Island, a recent study using foraminifera, testate amoeba, and plant macrofossils from a salt marsh to reconstruct late Holocene sea levels showed that RSL has been rising 1.3–2.0 mm/yr for the last two millennia, a rate slower compared to the more than 4.0 mm/yr experienced during the 20$^{th}$ century based on tide gauge data (Barnett et al., 2017). Recent work focused on the dating of beach dunes using optically stimulated luminescence has shown that many of these features developed over the last 2000–3000 years during this period of RSL rise, as sea water eroded sandstone cliffs, providing a source of sediment for local beaches and dunes (Rémillard et al., 2015). Indeed, some low-lying areas, including Havre-aux-Basques (a beach near one of the peatlands in our study) are still prograding, providing a constant source of sediment.

https://doi.org/10.5194/egusphere-2025-400
Preprint. Discussion started: 19 February 2025


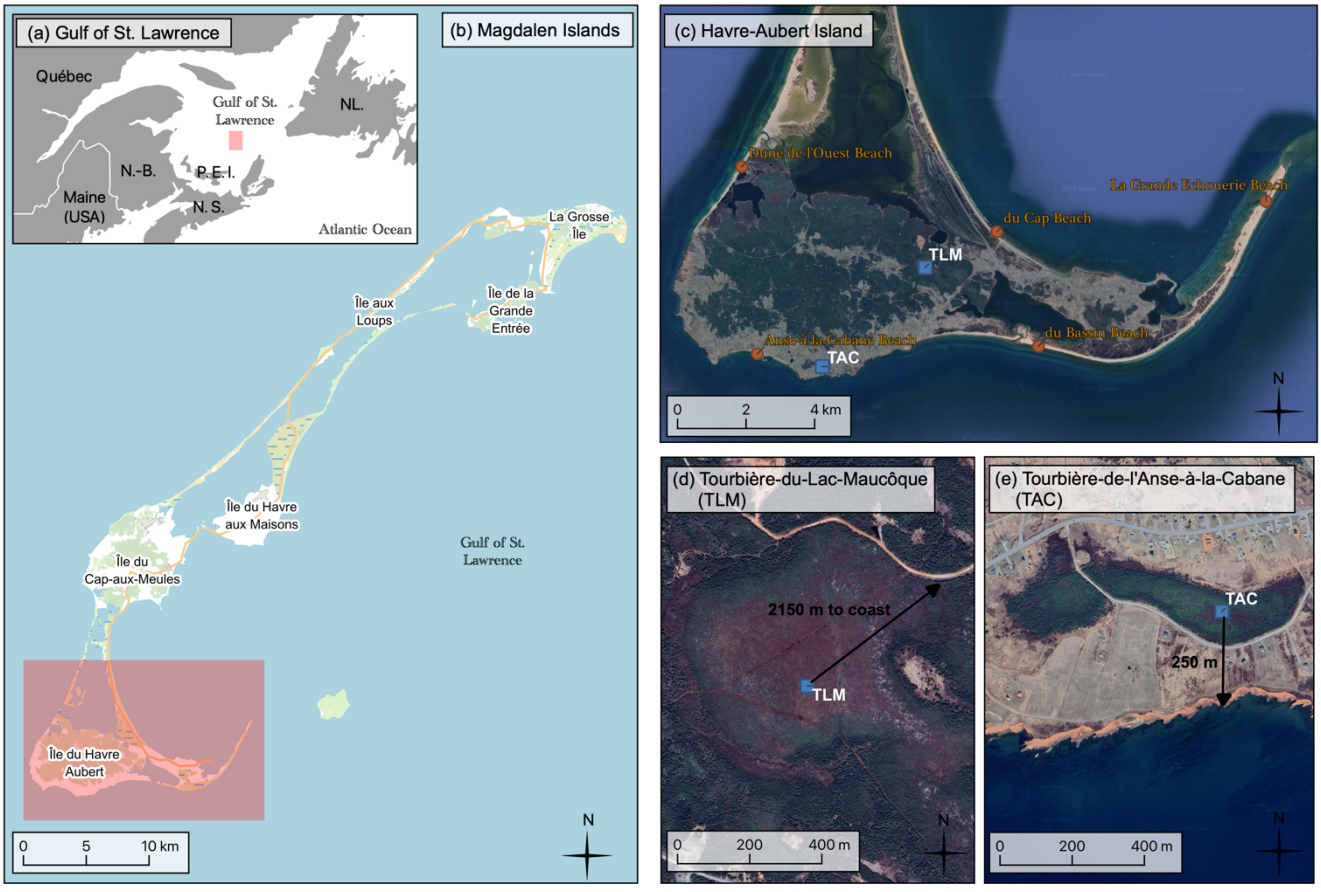


**Figure 1. Map and context of the study area. (a) The Magdalen Islands, located in the Gulf of St. Lawrence between Newfoundland and Prince Edward Island, in Atlantic Canada. The extent of map (b) is indicated by the red square. (b) The study site is on Havre-Aubert Island, the southernmost island of the archipelago. The extent of map (c) is indicated by the red square. (c) The two coring sites, Tourbière-du-Lac-Maucôque (TLM) and Tourbière-de-l'Anse-à-la-Cabane (TAC), are marked by blue squares, surrounded by multiple beaches, indicated by orange circles. (d, e) The TLM core site is 2150 m from the nearest beach (du Cap Beach), while the TAC core site is 250 m from south-facing sandstone cliffs. Imagery panel (b): © OpenStreetMap contributors, licensed under ODbL. Imagery panel (c–e): © Google Earth Pro 7.3.6.9796 (2024), Magdalen Islands, Quebec, Canada. Image date 22 April 2023, © 2025 Airbus.**

### 2.2 Study sites

We studied two peatbogs, *Tourbière-du-Lac-Maucôque* (TLM) (47°14' 30.9" N, 61°55' 24.7" W, ~4 m ASL) and *Tourbière-de-l'Anse-à-la-Cabane* (TAC) (47°12' 54.0"N, 61°57' 48.4"W, ~10 m ASL), located on Havre-Aubert Island, the southernmost island of the Magdalen Islands archipelago (Fig. 1a–c). TLM, a circular peatland with an area of 40.2 ha and an elevation 10 m above mean sea level, is situated approximately 2 km from coastal beaches on the south and northeast side of Havre-Aubert Island (Fig. 1d) (Ministère De L'environnement Et De La Lutte Contre Les Changements Climatiques, 2021a). TAC lies parallel to the coast, covers 9.0 ha, has an elevation between 18–21 m above mean sea level, and has its centre 250 m from the nearest south-facing red sandstone cliffs (Fig. 1d) (Ministère De L'environnement Et De La Lutte Contre Les

https://doi.org/10.5194/egusphere-2025-400
Preprint. Discussion started: 19 February 2025


Changements Climatiques, 2021b). Both sites are designated as protected areas by the *Gouvernement du Québec* due to their endangered populations of northern dwarf huckleberry (*Gaylussacia bigeloviana* [Fernald] Sorrie & Weakley), a small coastal shrub present at both locations. The dominant vegetation in the peatlands is *Sphagnum* spp. moss (Lindb.) and shrubs from the *Ericaceae* family, with black spruce (*Picea mariana* [Mill.] Britton, Sterns & Poggenburg) growing around the perimeter.

## 3 Methods

### 3.1 Core sampling

In August 2020, two peat cores were collected from each TLM and TAC using a Russian peat corer in 50 x 5 cm drives, near the centre of each peat dome to target the deepest and oldest peat (Fig. 1d–e). The two sequences at each site were less than 1 m apart and vertically offset by 25 cm. Due to low surface peat density, the top 0–50 cm monoliths were extracted using a shovel. Cores were stored in split PVC tubes and wrapped in cellophane, and monoliths were wrapped in cellophane, with all samples stored at 4° C at the Peros Lab at Bishop's University. The surface monoliths were compacted during transport and storage, requiring a correction factor of 1.79 (TLM) and 1.61 (TAC). This factor was calculated by dividing the original monolith length of 50 cm at the time of collection by the monolith length at the time of analysis. Continuous composite cores for each site were assembled by integrating core sequences with the surface monoliths (details in Appendix B).

### 3.2 Chronological controls

Twenty-five radiocarbon ($^{14}$C) dates (9 for TLM and 16 for TAC) were obtained from the A.E. Lalonde AMS Laboratory at the University of Ottawa, following the method described in Crann et al. (2017), and calibrated with the IntCal20 curve (Reimer et al., 2020) (Fig. 2 & Appendix C). Most samples submitted to AMS were terrestrial macrofossils, with some bulk peat samples included. Additionally, total lead-210 ($^{210}$Pb) activity was measured from 15 samples taken at regular intervals from the surface monoliths of TLM and TAC at the GEOTOP Radiochronology Laboratory at the *Université du Québec à Montréal* (UQAM), using an acid-digestion sequence and alpha spectrometry, adapted from De Vleeschouwer et al. (2010). The age-depth models for TLM and TAC were constructed using the Bayesian Plum model from the *rplum* package version 0.5.1 in R (Aquino-López et al., 2018; Blaauw et al., 2024), integrating the $^{14}$C and $^{210}$Pb dates. As $^{210}$Pb levels in the TLM monolith did not reach supported levels, the prior supported level from the TAC core was applied (supported mean = 17.5 Bq kg$^{-1}$) (Chartrand et al., 2023).

### 3.3 Peat identification

Peat type was identified using the Troels-Smith method (Troels-Smith, 1955). Samples of 1 cm$^3$ were extracted every 8 cm (TLM) and 4 cm (TAC) and examined under a stereoscopic microscope (at 4–40x magnification) to estimate the relative abundance of each peat type. Four main peat types were identified: bryophytic peat (dominated by *Sphagnum* spp. moss remains), herbaceous peat (dominated by sedge remains), ligneous peat (dominated by twigs and bark fragments), and humous

https://doi.org/10.5194/egusphere-2025-400
Preprint. Discussion started: 19 February 2025


peat (highly degraded peat with indistinguishable components). Mineral-rich layers and some macrofossils (seeds, leaves, needles) were also noted using the Continental Paleoecology Laboratory collection from GEOTOP at UQAM as reference (Garneau, 1995).

### 3.4 Loss-on-ignition and aeolian sand influx

Organic and mineral content in TLM and TAC were measured using loss-on-ignition (LOI) (Dean, 1974; Bengtsson and Enell, 1986; Heiri et al., 2001). Wet sediment samples (5 $cm^3$) were extracted every 2 cm (TLM) and every cm (TAC), dried overnight at 105 °C ($PEAT_{105}$) to calculate dry bulk density, then combusted at 550 °C ($ASH_{550}$) in crucibles with lids, with weights recorded at each step. Mineral content (%) was calculated as the ratio of $ASH_{550}$ to $PEAT_{105}$. The $ASH_{550}$ samples were treated with 10% hydrochloric acid (HCl) and 10% potassium hydroxide (KOH) to remove carbonate matter and deflocculate sediments (Vaasma, 2008), then sieved using a 63 µm sieve for TLM and a 125 µm sieve for TAC to establish the Aeolian Sand Influx (ASI) profiles. These size boundaries correspond to the fine/very fine sand (< 125 µm) for TAC and sand-silt (< 63 µm) for TLM (Wentworth, 1922), with a finer sieve for TLM due to its lower mineral content. ASI was calculated by multiplying sand density (g $cm^{-3}$) by the peat accumulation rate (cm $yr^{-1}$), and reported in g $m^{-2}$ $yr^{-1}$, as described by Björckl and Clemmensen (2004).

### 3.5 Micro X-ray fluorescence core scanning

We measured the inorganic geochemical compositions of TLM and TAC using an ITRAX Core Scanner (ITRAX–CS) from the *Laboratoire de géochimie, imagerie et radiographie des sediments* (GIRAS) at the *Institut national de recherche scientifique* (INRS) in Quebec City. Typically applied to marine and lacustrine sediments (Longman et al., 2019), the use of µ-XRF has recently been expanded to peat cores (Kern et al., 2019). Measurements were taken at 2 mm (TLM) and 1 mm (TAC) intervals using a Cr tube set to 40 kV, 10 mA and an acquisition time of 20 s. Our analysis focused on elements linked to terrigenous mineral inputs: K, Ti, Si, Fe, Mn, Ca, S.

### 3.6 Statistical analysis

#### 3.6.1 Data processing

The LOI and µ-XRF-CS datasets in this study are considered compositional data, as described by Aitchison (1982). Compositional data are non-negative, have a constant or irrelevant total sample size, and convey relative rather than absolute information, making direct application of statistical methods like clustering, correlation, and principal component analysis (PCA) inappropriate (Van Den Boogaart and Tolosana-Delgado, 2013; Bertrand et al., 2023). Therefore, µ-XRF and LOI variables are neither normally distributed nor independent, and require log-transformation for compatibility with conventional statistical methods (Van Den Boogaart and Tolosana-Delgado, 2013; Verhaegen et al., 2019). For µ-XRF intensities, centred-log-ratios (CLR) (Aitchison, 1982) were computed using Eq. (1) and Eq. (2) from Bertrand et al. (2023):

https://doi.org/10.5194/egusphere-2025-400
Preprint. Discussion started: 19 February 2025


$$clr\ A(z) = \ln\left[\frac{counts\ element\ A(z)}{g(z)}\right], \quad (1)$$

where $A(z)$ is the intensity of an element $A$ at depth $z$, and $g(z)$ is the geometric mean of all $n$ elements at depth $z$, calculated using Eq. (2):

$$g(z) = \sqrt[n]{counts_{element\ A(z)} \cdot counts_{element\ B(z)} \cdot \ldots counts_{element\ n(z)}}. \quad (2)$$

The computations were performed with the *clr* function in the *compositions* R package version 2.0-8 (Van Den Boogaart and Tolosana-Delgado, 2008; Van Den Boogaart et al., 2024). It is important to note that CLR calculations requires data free of zero values; therefore, zero values were infilled using a 10-points moving average.

For datasets with fewer than 5 components, such as the LOI dataset, CLR is unsuitable. Instead, these variables were log-transformed by taking the logarithm of the variable divided by the total (100%) minus the variable (e.g., $log\ (Minerals\ [\%]\ /\ (100 - Minerals\ [\%])\ )$ (Bertrand et al., 2023). Finally, ASI was log-transformed to meet the assumption of normality.

### 3.6.2 Statistical methods

Before consolidating the core drives into a composite core, we validated their alignment using cross-correlation analysis of overlapping raw µ-XRF measurements (Appendix B). Core zonation of TLM and TAC were determined using stratigraphically constrained cluster analysis (CONISS) from the *rioja* package version 1.0-7 in R (Juggins, 2024) on LOI and µ-XRF variables. To ensure consistency with LOI measurements, µ-XRF measurements were down-sampled to a 1 cm resolution prior to CLR transformation by averaging measurement every 1 cm. Correlation analyses were performed using Pearson's correlation coefficient to evaluate relationships among mineral content from LOI, ASI, and µ-XRF variables within each zone identified by CONISS. Principal component analysis (PCA) was conducted using seven elements of interest (K, Ti, Si, Fe, Mn, Ca, S), with mineral content and ASI included as passive variables. This analysis, performed with the *factoMineR* package version 2.11 in R (Husson et al., 2024), used z-score-transformed variables and a correlation matrix to compute the eigenvalues. Measurements from TLM and TAC's basal sand layers were excluded from all statistical analyses.

### 3.7 Paleo-storm identification

Two independent paleo-storm reconstructions were performed, one for each of TLM and TAC. Potential paleo-storm events were identified using detrended, raw µ-XRF Ti measurements, which served as an indicator of allochthonous lithogenic particle influx into the peat cores. Titanium emerged as the optimal high-resolution proxy for ASI, and consequently as a storm proxy, due to its consistent positive correlation with ASI in TLM and TAC (see Results). Titanium is a conservative element, resistant to biogenic processes and post-depositional re-working (Croudace and Rothwell, 2015), making it an ideal indicator of storm-derived sedimentation in peat. Early developmental stages of TLM and TAC, corresponding to fens conditions, were excluded from the storm reconstructions, as sediment delivery in these periods was likely dominated by non-aeolian processes (Sjöström et al., 2020). This storm detection methodology was applied separately to two periods: from 1851 to 2019 CE, and

https://doi.org/10.5194/egusphere-2025-400
Preprint. Discussion started: 19 February 2025


the pre-1851 CE period, to account for the increased sediment delivery observed during the most recent period, likely linked to direct human activities.

To identify intervals where Ti exceeded background levels, we used an approach adapted from Donnelly et al. (2015) and Lane et al. (2011). First, to account for variations attributed to long-term lithogenic changes, we detrended Ti using a running average using Eq. (3):

$$Ti_{detrended}(z) = Ti_{raw}(z) - RA_{Ti}(z, w), \quad (3)$$

where $RA_{Ti}(z, w)$ is the running average of raw Ti at depth $z$, calculated over a window length $w$: 10 years for the period 1851-2019 CE and 30 years for the period pre-1851 CE, reflecting the higher peat accumulation rate during the modern period.

The threshold for identifying outlier Ti values was defined with the Tukey Rule of outlier detection (Tukey, 1977), following Winkler et al. (2020):

$$Ti_{threshold} = Q_{0.75}(Ti_{detrended} > 0) + x \cdot IQR(Ti_{detrended} > 0), \quad (4)$$

where $Q_{0.75}(Ti_{normalized} > 0)$ is the third quartile of detrended Ti values above zero, and $x \cdot IQR(Ti_{normalized} > 0)$ is the interquartile range of detrended Ti values above zero, multiplied by a factor $x$ of 0.75 for TLM and 1.5 for TAC, respectively. The lower $x$ value for TLM accounts for its reduced Ti variability related to TAC as it is further from the coast. Detrended Ti values exceeding the threshold were considered storm events. To avoid overestimating the number of events due to consecutive Ti measurements associated with a single Ti peak, consecutive measurements were grouped together, and only the maximum value within each group was retained in the final paleo-storm record. Finally, the number of events per century was calculated using a 100-year running-sum.

### 3.8 Historical storm record and compilation

We used the *International Best Track Archive for Climate Stewardship* (IBTrACTS) dataset (Knapp et al., 2010; Gahtan et al., 2024) to determine the number of cyclones with a tropical origin passing within 100 km of the Magdalen Islands from 1851 to 2019 CE. To assess the impact of these storms on the Magdalen Islands, we cross-referenced the IBTrACTS data with historical shipwrecks records and local newspaper archives. We searched the online press database of the *Bibliothèque et Archive National du Québec* (Bibliothèque Et Archive Nationale Du Québec, 2024) using French keywords such as *ouragan* and *Iles-de-la-Madeleine*, and notes were taken on storm-related damage in the Magdalen Islands. Additionally, we manually reviewed shipwreck records from the vicinity of the Magdalen Islands (Landry, 1989, 1994) for incidents attributed to storms identified in the IBTrACTS dataset. Storms mentioned in the newspaper articles or shipwreck records that were not present in the IBTrACTS dataset, but that had significant impacts on the Magdalen Islands, were added to the final historical storm dataset.

https://doi.org/10.5194/egusphere-2025-400
Preprint. Discussion started: 19 February 2025


## 4. Results

### 4.1 Chronostratigraphy

The TLM composite core measured 700 cm, with a basal sand layer between 693–700 cm. The TAC composite core was 325 cm long, with a basal sand layer between 317–325 cm (see Appendix D for core photographs). The age-depth models indicated that organic accumulation began above the basal sand layers around 2960 BCE for TLM and 2900 BCE for TAC, giving an approximate chronology of 5000 years of peat accumulation for both cores (Fig. 2). The average peat accumulation rate (PAR) was 0.17 cm $yr^{-1}$ for TLM and 0.12 cm $yr^{-1}$ for TAC. At TAC, an abrupt decrease in PAR to 0.02 cm $yr^{-1}$ occurred between 135–159 cm (870 CE–870 BCE), suggesting a pronounced reduction in peat accumulation or a hiatus. This trend was not observed in TLM. In the upper 50 cm of both cores, which includes the acrotelm (the layer containing living plants) and was dated using $^{210}$Pb, the PAR increased significantly to 0.77 cm $yr^{-1}$ for TLM and 0.29 cm $yr^{-1}$ for TAC. Further details about the chronostratigraphy can be found in Appendix C.

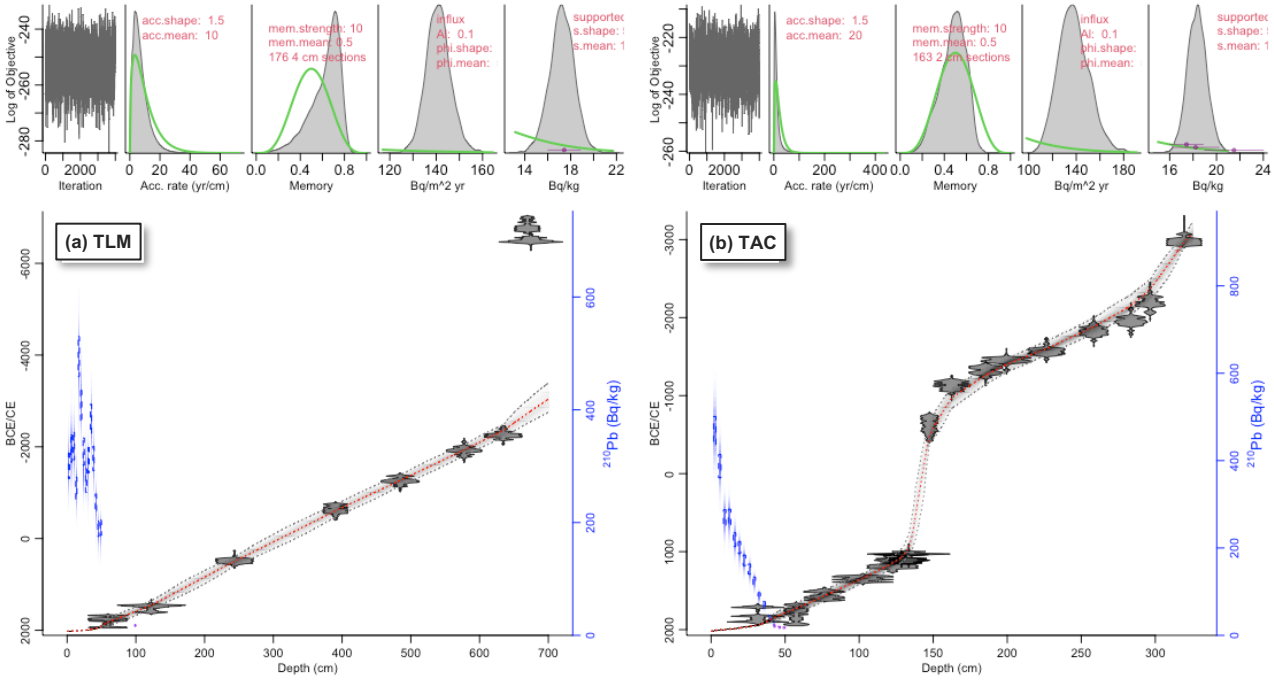


**Figure 2.** ***rplum*-derived age-depth models for TLM (a) and TAC (b). Radiocarbon ($^{14}$C) dates are shown in grey along the mean age model (dotted red). The rate of supported $^{210}$Pb (right axis) is indicated by blue boxes on the left side (the blue boxes are the measured $^{210}$Pb values, while the blue shadings represent the modelled $^{210}$Pb values). A blown-up version of the $^{210}$Pb diagrams is available in Fig. C1. For each core, the upper left panel shows the Markov Chain Monte Carlo (MCMC) iterations; followed by the prior (green curve) and posterior (grey histogram) distributions for the accumulation rate (second panel), memory (third panel), $^{210}$Pb influx in Bq/m$^2$·yr (fourth panel) and supported $^{210}$Pb in Bq/kg (fifth panel). Since $^{210}$Pb levels in TLM did not reach supported levels, the prior supported level from the TAC (s. mean = 17.5 Bq $kg^{-1}$) core was used.**

https://doi.org/10.5194/egusphere-2025-400
Preprint. Discussion started: 19 February 2025


### 4.2 Downcore variations in lithology

The TLM core was divided into three zones (Fig. 3a). Zone 1 (692–565 cm, 2950–1840 BCE) consisted mainly of ligneous peat with a high mineral content of 13 % and a mean ASI of 3.4 g $m^{-2}$ $yr^{-1}$. This zone included seeds from *Menyanthes trifoliata* L. (bog bean), a common shallow-water plant (Magnan et al., 2014). A detritus peat layer between 657–652 cm (2590–2535 BCE) contained a peak mineral content of 34 %. Zone 2 (565–452 cm, 1840–1035 BCE) transitioned from ligneous to herbaceous peat with a sharp decrease in mineral content to an average of 2.3 % and an ASI of 0.06 g $m^{-2}$ $yr^{-1}$. There was an abrupt transition to bryophytic peat at 486 cm (1280 BCE). Zone 3 (450–0 cm, 1035 BCE–2019 CE) showed clear ombrotrophic conditions (Fig. 3) and alternated between well-preserved and degraded bryophytic peat, with a low mineral content of 1.5 % and a mean ASI of 0.1 g $m^{-2}$ $yr^{-1}$. The upper 50 cm showed a higher mineral content (2.5 %) and ASI (0.6 g $m^{-2}$ $yr^{-1}$).

The TAC core was divided into 4 zones (Fig. 3b). Zone 1 (316–274 cm, 2890–2050 BCE) consisted of herbaceous peat interspersed with small ligneous fragments. It had a moderate mineral content of 6 % and a mean ASI of 0.15 g $m^{-2}$ $yr^{-1}$. A sand-enriched layer (28 % mineral content) between 309-305 cm (2700–2590 BCE) coincided chronologically with a similar layer in TLM. *Sphagnum* macrofossils first appeared at 284 cm (~ 2160 BCE). Zone 2 (274–159 cm, 2050–880 BCE) showed ombrotrophic conditions and alternated between well-preserved and degraded bryophytic peat, with the lowest mineral content (3 %) and ASI (0.08 g $m^{-2}$ $yr^{-1}$). Zone 3 (159–135 cm, 880 BCE–870 CE) was a dense, mineral-rich zone (minerals content 27% and ASI 8.1 g $m^{-2}$ $yr^{-1}$) dominated by detritus peat with ligneous layers. It contained two fine-grained sand layers at 151 cm (~ 600 BCE) and 136 cm (~ 810 CE), with mineral contents of 32 % and 55 %, respectively. Due to a high degree of peat degradation, ombrotrophic conditions could not be confirmed for Zone 3. However, ombrotrophic conditions were re-established in Zone 4 (135–0 cm, 870–2019 CE), which consisted of well-preserved bryophytic peat with a mineral content of 21% and the highest ASI at 3.6 g $m^{-2}$ $yr^{-1}$.

https://doi.org/10.5194/egusphere-2025-400
Preprint. Discussion started: 19 February 2025


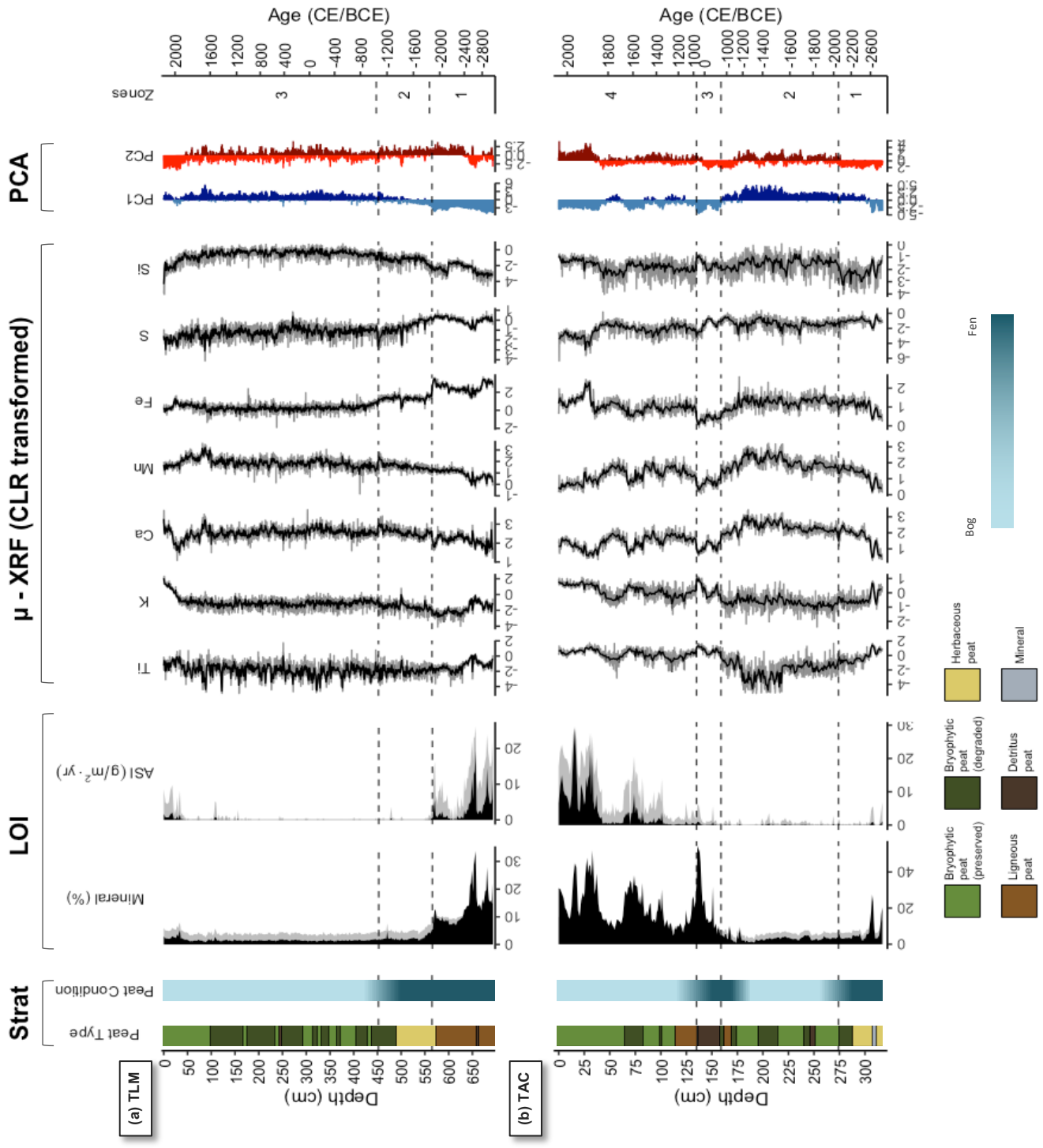

https://doi.org/10.5194/egusphere-2025-400
Preprint. Discussion started: 19 February 2025


**Figure 3. Lithological and geochemical profiles of the TLM (a) and TAC (b) composite cores. The peat type (bryophytic, herbaceous, ligneous, detritus, mineral) is color-coded, along with peatland classification (bog versus fen). Grey shading in the LOI variables correspond to the $log_{10}$ of the mineral content and ASI to enhance visualization of small variations. Micro–XRF variables are displayed as CLRs. Grey lines indicate the µ–XRF original resolution (2 mm for TLM and 1 mm for TAC), while the black lines represent data averaged to 1 cm intervals. The first two principal components (PCA 1 and PCA 2) performed on seven CLR-transformed µ-XRF elements are presented. Dark blue/red indicate positive loading, while pale blue/red indicate negative loading.**

https://doi.org/10.5194/egusphere-2025-400
Preprint. Discussion started: 19 February 2025


### 4.3 Principal component analysis and geochemical profiles

Only statistically significant results are described. The first principal components (PC1), derived from the PCA of seven elements of interest (K, Ti, Si, Fe, Mn, Ca, S) and two passive variables (mineral content and ASI), explained 49 % and 52 % of the total data variance at TLM and TAC, respectively (Fig. 3). At both sites, PC1 was strongly negatively correlated with mineral content (TLM: $r$ = -0.95; TAC: $r$ = -0.92) and ASI (TLM: $r$ = -0.92, TAC: $r$ = -0.85), indicating that positive PC1 corresponded to low mineral/high organic content, and negative PC1 indicated high mineral/low organic content. At TLM, PC1 showed the strongest negative correlations with Fe ($r$ = -0.84) and S ($r$ = -0.71), linking these elements to mineral content and ASI. In contrast, at TAC, PC1 was most strongly negatively correlated with Ti ($r$ = -0.90) and K ($r$ = -0.75), highlighting differences in the main geochemical composition between the two sites. However, PC1 at both locations was positively correlated with Mn and Ca, reflecting the consistent association of those elements with low mineral content. The second principal components (PC2) explained 21 % and 19 % of the variance in TLM and TAC, respectively, and showed no strong correlation with mineral content or ASI. At TLM, PC2 was positively correlated with S ($r$ = 0.54), Ca ($r$ = 0.44), and Fe ($r$ = 0.29), and negatively correlated with Ti ($r$ = -0.72) and K ($r$ = 0.60). At TAC, PC2 was positively correlated with Si ($r$ = 0.55), Fe ($r$ = 0.57), and K ($r$ = 0.35), and negatively correlated with S ($r$ = -0.81). In both cases, PC2 likely reflected variations in the geochemical composition associated with changes in sources of mineral input.

Zone 1 of TLM (692–565 cm, 2950–1840 BCE) saw a shift in chemical composition indicated by PC2: Ti and K dominated the older (lower) part, while Fe, S, and Ca, commonly measured in higher proportion in fens (Shotyk, 1988), increased in the upper section. This shift corresponded to the detritus layer at 657–652 cm (2590–2535 BCE). In Zone 2 (565–452 cm, 1840–1035 BCE), PC2 remained positive, reflecting higher proportions of Fe and S, which are positively correlated with mineral content in that zone (Table E1). Zone 3 (450–0 cm, 1035 BCE–2019 CE) showed alternating PC2, indicating variable contributions from Ti, K, Fe, S, and Ca, though only Ti, K, and Fe were significantly positively associated to mineral content and ASI in this zone (Table E1). In the upper 50 cm, a negative shift in PC2 highlighted a dominance of Ti and K in modern sediment inputs.

At TAC, Zone 1 (316–274 cm, 2890–2050 BCE) saw a shift in chemical composition indicated by PC1, with Ti and K dominating the older (lower) part, while Fe, Mn and Ca became more prominent in the upper part. As with TLM, this shift was associated to a sand-enriched layer. A negative PC2 indicated a high S content, though S showed no significant correlation with mineral content (Table E1). In Zone 2 (274–159 cm, 2050–880 BCE), only Ti showed a positive correlation with the mineral content (Table E1). Zone 3 (159–135 cm, 880 BCE–870 CE) contained fine-grained layers enriched in Ti, K, and Si, as indicated by strong positive correlations with mineral content, and a negative PC2 suggested the presence of S, though it was not associated to mineral content (Table E1). In Zone 4 (135–0 cm, 870–2019 CE), LOI variables were positively correlated with Ti, K, and Fe, while in the upper 50 cm, a positive PC2 reflected increased input of Fe and Si.

https://doi.org/10.5194/egusphere-2025-400
Preprint. Discussion started: 19 February 2025


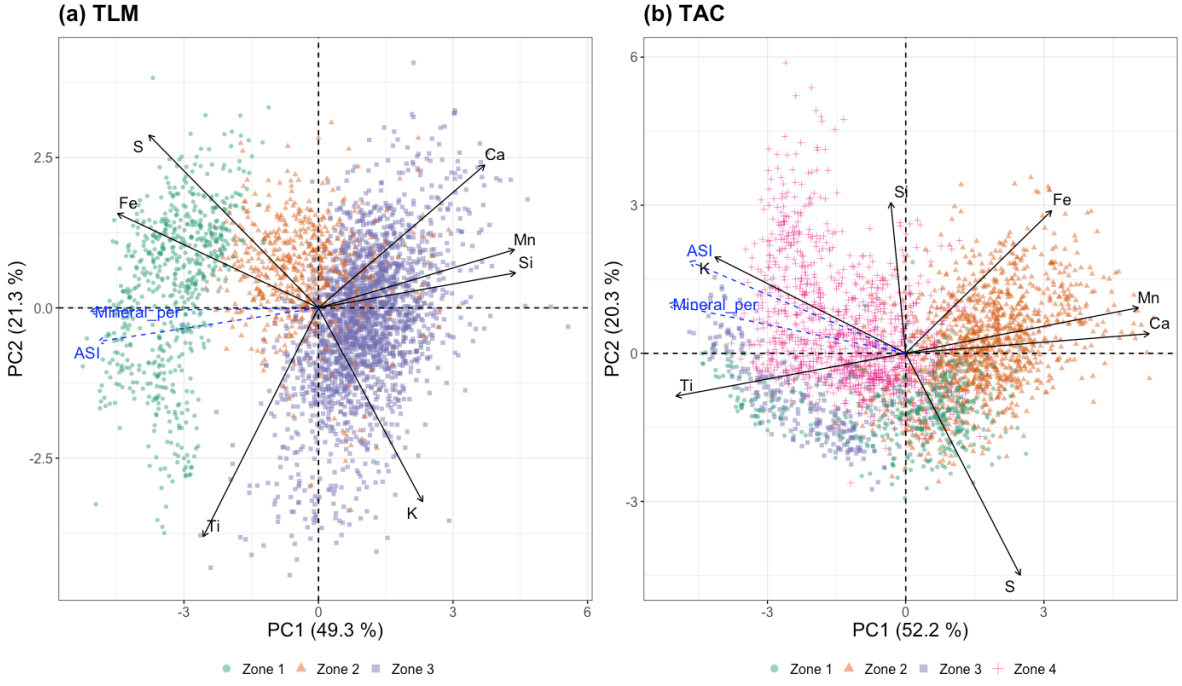


| PC | 1 | 2 |
|---|---|---|
| % variance | 49.3 | 21.3 |
| | correlations *r* | |
| **Ti** | **-0.48** | **-0.71** |
| **K** | **0.43** | **-0.60** |
| **Si** | **0.82** | 0.11 |
| **Fe** | **-0.84** | **0.29** |
| **Mn** | **0.82** | 0.18 |
| **Ca** | **0.69** | **0.44** |
| **S** | **-0.71** | **0.54** |
| **Minerals** | **-0.95** | 0 |
| **ASI** | **-0.92** | -0.10 |

| PC | 1 | 2 |
|---|---|---|
| % variance | 52.3 | 19.4 |
| | correlations *r* | |
| **Ti** | **-0.90** | -0.15 |
| **K** | **-0.75** | **0.35** |
| **Si** | **-0.36** | **0.55** |
| **Fe** | **0.57** | **0.52** |
| **Mn** | **0.91** | 0.16 |
| **Ca** | **0.96** | 0.07 |
| **S** | **0.45** | **-0.81** |
| **Minerals** | **-0.92** | 0.18 |
| **ASI** | **-0.85** | 0.33 |

**Figure 4. Principal components analyses (PCA) of the seven µ-XRF elements for TLM (a) and TAC (b). Each CONISS zone is depicted with a distinctly coloured symbol. Solid black arrows represent the µ-XRF variables used in the PCA, while dashed blue arrows represent the supplementary variables (Minerals and ASI). The Pearson correlation coefficients *r* between the principal components and all variables are displayed below the respective biplots, with significant correlations *r* +/- 0.2 highlighted in bold.**

https://doi.org/10.5194/egusphere-2025-400
Preprint. Discussion started: 19 February 2025


### 4.4 Paleo-storm reconstructions

We did two separate paleo-storm reconstructions based on Ti measurements, one for each site. The TLM paleo-storm reconstruction (Fig. 5a) was based on its Zone 3 (1035 BCE–2019 CE; ~ 3050 years), while the TAC paleo-storm reconstruction (Fig. 5b) was based on its Zones 2–4 (2050 BCE–2019 CE; ~ 4070 years). Zones 1–2 of TLM and Zone 1 of TAC were excluded, as they each corresponded to early peat development stages when wetlands and/or fens conditions probably prevailed. Sediment delivery during these early periods was likely driven by non-aeolian processes, making them unsuitable for storm reconstruction. Additionally, the TAC core contained two fine-grained sand layers at 151 cm (600 BCE) and 136 cm (810 CE) (Zone 3, Fig. 3b) that corresponded to a very slow peat accumulation period or a hiatus (Fig. 2b). While similar sand deposits were not visible in TLM, the Ti data for this section of TAC (Fig. 5b) closely mirrored TLM's trend of events per century during the same interval (Fig. 5a), with heightened values between 800–600 CE and 600–900 BCE. Therefore, although this section of TAC lacked clear ombrotrophic conditions, we included it in our paleo-storm analysis due to its close similarity with the TLM data.

In TLM, the event thresholds were 63.6 Ti cps (1851–2019 CE) and 41.6 cps (pre-1851 CE) above the Ti moving average. Since 1035 BCE, the detrended Ti record exceeded the event threshold 66 times (Fig. 5a), yielding an average frequency of 2.3 events per century. Five periods exceeded the record's average events per century: 770–535 BCE, 605–800 CE, 1220–1320 CE, 1390–1785 CE, and 1955–2019 CE, with a maximum of ~ 6 events per century.

For TAC, the event thresholds were 917.3 cps (1851–2019 CE) and 283.6 cps (pre-1851 CE) above the moving average. Since 2050 BCE, the detrended Ti exceeded the event threshold 70 times (Fig. 5b), corresponding to an average of 2.3 events per century. Four periods exceeded the record's average frequency: 835–685 BCE, 1315–1710 CE, 1750–1840 CE and 1880–2002 CE. Notably, TAC recorded a peak storm activity period centred around 1600 CE, with nearly 14 events per century, while the other periods exhibited 3–6 events per century. Importantly, the very low peat accumulation rate in TAC Zone 3 (135–159 cm, 880 BCE–870 CE) meant that the events per century during this time was almost certainly underestimated.

Overall, the events per century reconstructions for both sites were remarkably similar, indicating enhanced mineral input to both peatlands, and hence storminess, during three main periods: 800-550 BCE, 600-800 CE, and 1300-1700 CE.

https://doi.org/10.5194/egusphere-2025-400
Preprint. Discussion started: 19 February 2025


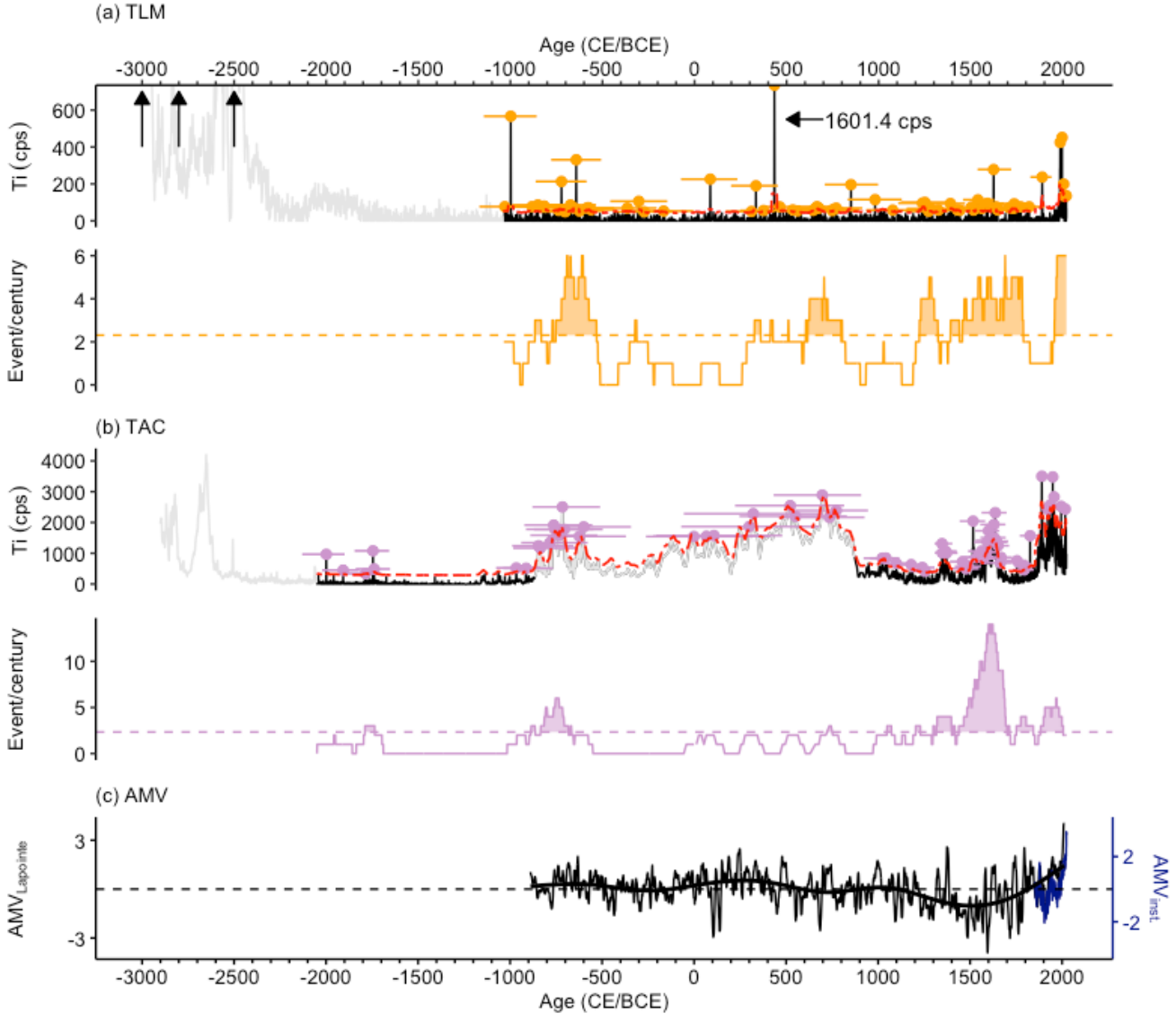


370 **Figure 5. Titanium (Ti) counts per second (cps) and storm event per century for TLM (a; in orange) and TAC (b; in purple). Solid vertical black lines in (a) and (b) show raw Ti µ-XRF measurments during the periods of storm reconstruction, corresponding to the ombrotrophic portions of the core. Grey lines indicate the non-ombrotrophic portions of the cores, excluded from the reconstruction (except for the period correponding to Zone 3 in TAC). Dashed red lines indicate the moving thresholds of event detection, calculated using the Tukey rule over a moving average (see Methods for details). Events are marked by orange (TLM)**
375 **and purple (TAC) dots, with horizontal bars representing age uncertainty. Event frequencies are shown as a 100-year moving sum, with the average number of events per century shown as horizontal dashed lines. (c) The annually-resolved Atlantic Multidecadal Variability (AMV) reconstruction based on titanium measurements from a varved lake record from Ellesmere Island, in Arctic Canada. An instrumental AMV record (1854–2023) is shown in dark blue (Huang et al., 2017).**

https://doi.org/10.5194/egusphere-2025-400
Preprint. Discussion started: 19 February 2025


## 5. Discussion

### 5.1 Key similarities and differences between TLM and TAC

TLM and TAC showed storm signals that were generally consistent, suggesting that peatbogs can serve as reliable archives for paleo-storm reconstructions. Our reconstructions revealed three main periods of enhanced storm activity shared by both sites: 1300–1700 CE, 600–800 CE, and 800–550 BCE. However, notable differences in mineralogy and geochemistry between the two cores deserve further considerations to improve the interpretation of storm records.

#### 5.1.1 Peat development

The development of peat at TLM and TAC reflects contrasting formation processes, hydrological sensitivities, and sedimentary influences, highlighting differences in their initial formation, later transitions, and responses to climatic and local environmental changes. The fen-to-bog transition in TLM and TAC was characterized by the increasing dominance of *Sphagnum* mosses and a positive correlation between mineral content and lithogenic elements such as Ti and K. However, the timing of this transition differed substantially, with TAC transitioning around 2050 BCE and TLM following over a millennium later, around 1000 BCE. This temporal discrepancy may reflect differences in the initial conditions of peat formation at each site. At TLM, the presence of *Menyanthes trifoliata* seeds within mineral-rich ligneous peat suggests that the site initially formed through the terrestrialization of a shallow water body (Hewett, 1964; Kuhry and Turunen, 2006). In contrast, the basal peat at TAC, composed of mostly herbaceous remains and lacking *Menyanthes trifoliata* seeds, suggests that the peatland formed directly on a mineral substrate in a well-drained environment, likely through primary paludification — a direct shift from bare land to peatland, without an intermediary wetland step (Kuhry and Turunen, 2006). Additionally, the smaller size of TAC, which currently extends over 9 ha compared to TLM's 40 ha, likely rendered it more sensitive to hydrological changes, such as the sharp increase in mineral content around 2600 BCE, as has been found in a study from Sweden (Sjöström et al., 2020). This interpretation is further supported by TAC's lower peat accumulation rate, shallower $^{210}$Pb profile, and lower $^{210}$Pb influx compared to TLM, suggesting that TAC is more exposed, has reduced snow accumulation, and, consequently, has more unstable hydrological conditions (Perrier et al., 2022).

Another notable difference in peat development was the presence of distinct sand layers at TAC at depths corresponding approximately to 600 BCE (151 cm) and 810 CE (136 cm), which are absent at TLM. The lack of abrupt contacts between the sand and the underlying and overlying peat (Appendix D) supports the interpretation that these units represent gradual accumulations of sand over time rather than short-lived deposition events. The presence of such prominent sand-layers may be due in part to the proximity of TAC to the coast and a sediment source (Fig. 1e). However, a more likely explanation is that these units represent an *in-situ* concentration of mineral matter due to a period of enhanced peat decomposition, possibly related to a change in hydrology that affected only TAC. Its relatively small size and its orientation perpendicular to a downward-sloping elevation gradient may have rendered this site more sensitive to changes in groundwater flow compared to TLM. The beginning of this period of slow peat accumulation coincided with the 2.8 ka event, which was a

https://doi.org/10.5194/egusphere-2025-400
Preprint. Discussion started: 19 February 2025


centennial-scale period generally characterized by cool and often dry conditions in the circum-North Atlantic (Van Geel et al., 1996). Just to the south, Baltic Bog, at Prince Edward Island, experienced a period of reduced peat accumulation or a hiatus around this time (Peros et al., 2016), and a similar event is recorded at a peatland in the Netherlands (Van Geel et al., 2014). While the specific mechanism behind the formation of these sand layers remains unclear, their timing and context suggest a complex interplay between local hydrology and broader climatic changes, necessitating further investigation.

### 5.1.2 Aeolian sediment sources

TLM and TAC exhibited distinct patterns in aeolian sediment input, reflecting differences in their proximity to sediment sources and local geological settings. TLM consistently displayed lower mineral content than TAC, particularly during ombrotrophic periods. For instance, in the modern period (post–1851 CE), ASI values at TLM were an order of magnitude smaller than those at TAC, even after adjusting the grain-size threshold to 63 µm for TLM compared to 125 µm for TAC (Fig. 3). This disparity likely reflects TLM's greater distance from sediment sources: TLM is situated 2 km from the nearest beach, while TAC is only 210 m from south-facing sandstone cliffs (Figs. 1d–e). The surface geology of the Magdalen Islands suggests that aeolian sediments in this region primarily originate from local beaches and sandstone cliffs, which are rich in quartz ($SiO_2$), k-feldspar ($KAlSi_3O_8$), and Ti-bearing minerals from basaltic rocks (Brisebois, 1981; Sabina, 2003; Rémillard et al., 2016). While both cores showed a strong association between ASI and both Ti and K – elements common in sandstone and beach-derived sediments — the geochemical signature diverged during the modern period. At TAC, the positive correlation of Si and Fe with ASI and mineral content (Table E1) supports the interpretation that sandstone cliffs serve as the primary sediment source. Silicon is enriched in coarser grain-size fractions (Liu et al., 2019), which are more likely to be transported over short distances during storms. Furthermore, the sandstone cliffs are rich in hematite-($Fe_2O_3$)-coated quartz (Sabina, 2003), which would explain the elevated Fe content at TAC. In contrast, TLM's sediment appeared to be derived primarily from sand beach sands, which are depleted in hematite, and is consistent with the site's greater distance from the sandstone cliffs. Ti emerged as the common aeolian sand indicator in both TLM and TAC. While Ti and K consistently correlated with ASI in both cores, K, as an essential plant nutrient, can accumulate in plant tissues, potentially complicating its interpretation as aeolian sand. This likely explains the increase in K observed in the upper 50 cm at TLM (Fig. 3a), further supported by its positive correlation with Ca, another essential plant nutrient, also in the acrotelm (Table E1).

### 5.1.3 Aeolian grain-size and associated wind speed

The minimum grain sizes of 63 and 125 µm for the ASI measured at TLM and TAC, respectively, provide insights into the minimum wind speeds required to entrain and transport this material into each peatland. Wind speed thresholds for sediment transport depend on factors such as surface moisture and cohesion, topography and vegetation, and distance between sediment sources and deposition sites (Pye and Tsoar, 2008; Goslin et al., 2019). At both TLM and TAC, the primary sediment sources – sandstone cliffs and beaches – are relatively unconsolidated, and the intervening terrain is flat and at a similar elevation. For the > 125 µm size fraction measured at TAC, wind speeds of more than 22.5 m $s^{-1}$ (~80 km $h^{-1}$) are needed to

https://doi.org/10.5194/egusphere-2025-400
Preprint. Discussion started: 19 February 2025


transport sand in suspension (Pye and Tsoar, 2008). The threshold for the > 63 μm fraction recorded at TLM is lower, but the greater distance from beaches to TLM (Fig. 1) likely necessitates stronger winds. These grain-size characteristics suggest that the sand fractions at both sites were deposited during high-magnitude storm events, consistent with wind speeds recorded during major fall and winter storms in the region (Fig. 6c), further supporting the use of ASI, and by extension Ti, as a proxy for storm activity.

### 5.2 Modern storm attribution (1851-2019 CE)

To validate the relationship among ASI, Ti, and storm events, ASI and Ti data were compared with storm tracks and intensities from the IBTrACS hurricane dataset (1851-2019 CE) (Knapp et al., 2010; Gahtan et al., 2024). The strongest storms affecting the Magdalen Islands are tropical cyclones, which typically track towards the north and northeast above or near the Bahamas Archipelago, and parallel to the eastern seaboard of North America, before entering the Gulf of St. Lawrence as post-tropical cyclones and dissipating over the North Atlantic (Fig. 6a). Since 1851 CE, 38 such events have passed within 100 km of the Magdalen Islands, with many producing wind speeds in the 75–125 km $h^{-1}$ range (Fig. 6, Appendix F). Of these, six had significant impacts, the most recent being Hurricane Dorian on September 7, 2019 (Jardine et al., 2021). Additionally, nor-easters — mid-latitude winter storms originating along the US eastern seaboard — frequently affect the region, bringing northeast winds exceeding 100 km $h^{-1}$ and occurring at a frequency of 2–3 per decade (Forbes et al., 2004; Hundecha et al., 2008; Bernatchez et al., 2012). Finally, winter westerlies storms forming over the Central Rockies mountains and the Great Lake region also affect the Magdalen Islands, though these storms typically dissipate over eastern Canada (Plante et al., 2015).

The ASI and Ti record for 1851-2019 CE (Figs. 7a-b) show notable correspondence between the two sites, particularly two large peaks in ASI dating to approximately 1985 and 2010 and a peak in Ti circa 1887. However, TAC exhibits elevated ASI and Ti between 1915–1970, unlike TLM. The larger size of TLM and its greater distance to mineral sources (Fig. 1) likely explains this discrepancy, though regional differences in human activity, such as gravel road construction near TAC during this period (Fortin and Larocque, 2003), may have also contributed.

The relationship among ASI, Ti, and IBTrACS data (Fig. 7a–c) is more complex. For instance, the most recent major storm, Hurricane Dorian (2019), may be evident in the first ASI and Ti peak at TLM right at the surface, but there is no clear signal for it in TAC, despite it coming ashore. Alternatively, downward movement of sediments in the spongey peat matrix may have dated sediments associated to Hurricane Dorien to an older interval, perhaps the peak centred around 2010. At TLM, the Ti peak circa 1995 may correspond to a nor'easter on November 7, 1994, while peaks in ASI and Ti around 1990 may reflect the winter storms from December 16, 1990, or December 4, 1989, all of which had severe local impacts (Bernatchez et al., 2012). At TAC, one of these storms may correspond to the Ti and ASI peaks around 1990. Earlier, the mineral increase and Ti peaks from 1915–1970 align with a cluster of storms from the IBTrACS data, and elevated Ti between 1870–1900 coincides to a series of storm events during that same period. Finally, the prominent peak in Ti around 1888 in TAC and 1886 in TLM may represent the August Gale of 1873, one of the most destructive storm to hit the Magdalen Island in the historical records (Landry, 1989, 1994).

https://doi.org/10.5194/egusphere-2025-400
Preprint. Discussion started: 19 February 2025


Attributing specific storms to Ti or ASI peaks in peat records remain challenging due to large age uncertainty and the potential downward movement of mineral particles in peat, which can blur deposition signals. Additionally, it seems that not all major events are captured; for instance, Hurricane Blanche in 1975 (Public Safety Canada, 2024) is not evident in either the TLM or TAC records. As mentioned above, nor'easter and winter westerly storms may contribute to some peaks in the record, though their effect depends on snow and ice cover, which could limit sediment entrainment. Overall, we interpret the Ti and ASI records in both cores to primarily represent summer and fall storm activity, with some contribution from early winter storms. Nevertheless, as will be seen below, our records are strikingly similar to those from regions impacted exclusively by tropical cyclones.

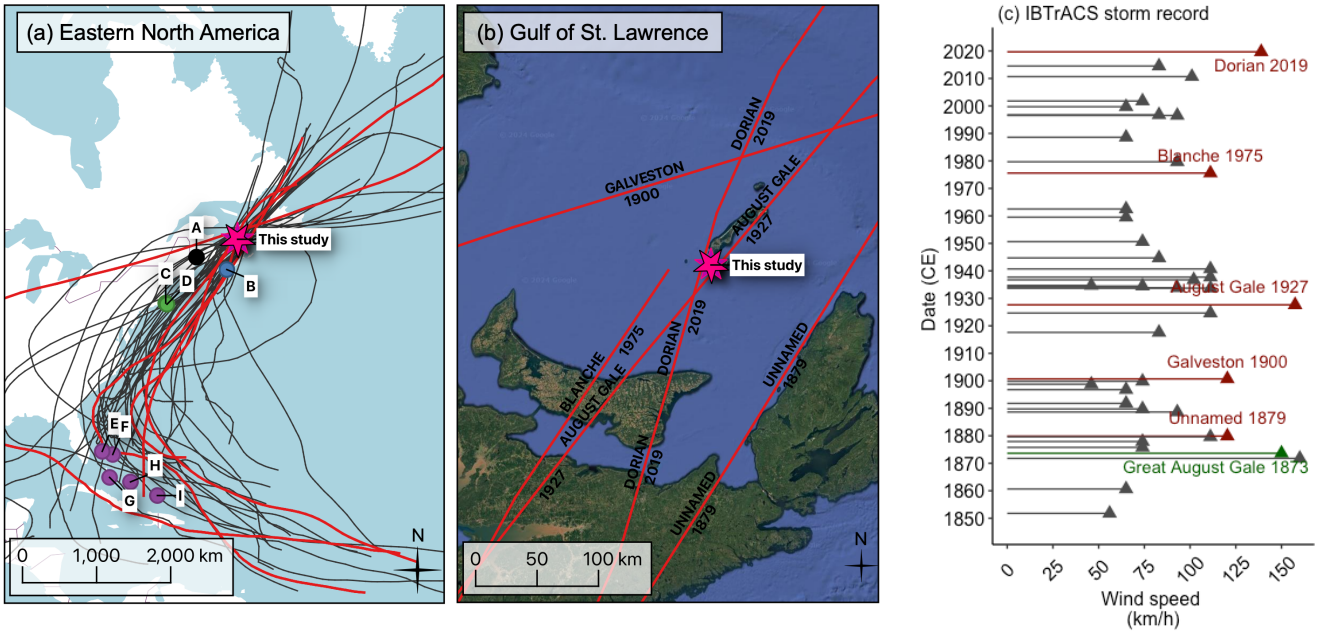


**Figure 6. (a) Map showing the location of the Magdalen Islands (pink star — this study) and tracks of storms passing within 100 km, based on the IBTrACKS dataset from 1851–2019 CE (Knapp et al., 2010; Gahtan et al., 2024). Storms known to have impacted the Magdalen Islands are highlighted in red. Some paleo-storm records referenced in this paper are marked on the map: A (green circle) — Robinson Lake, New Brunswick, Canada (Patterson et al., 2022); B (orange circle) — Robinson Lake, Nova Scotia, Canada (Oliva et al., 2017); C and D (blue circles) — Mattapoisett Marsh (Boldt et al., 2010) and Salt Pond, Massachusetts (Donnelly et al., 2015); E–I (purple circles) — the studies compiled in the Bahamas compilation: Grand Bahamas (Winkler et al., 2023), Thatchpoint Blue Hole, Abaco Island (Winkler et al., 2020), South Andros (Wallace et al., 2019), Long Island (Wallace et al., 2021b), and Middle Caicos (Wallace et al., 2021a). (b) Enlarged view of the Magdalen Islands region, showing storm tracks with documented local impacts. (c) Bar chart showing peak winds (km $h^{-1}$) of the storms indicated in panels (a) and (b) as they passed within 100 km of the Magdalen Islands. The Great August Gale of 1873, highlighted in green, was not in the IBTrACS dataset, but had known impacts on the Magdalen Islands. Imagery panel (b): © Google Earth Pro 7.3.6.9796 (2024), Gulf of St. Lawrence, Canada. Image date 31 December 2023, © Landsat/Copernicus.**

https://doi.org/10.5194/egusphere-2025-400
Preprint. Discussion started: 19 February 2025


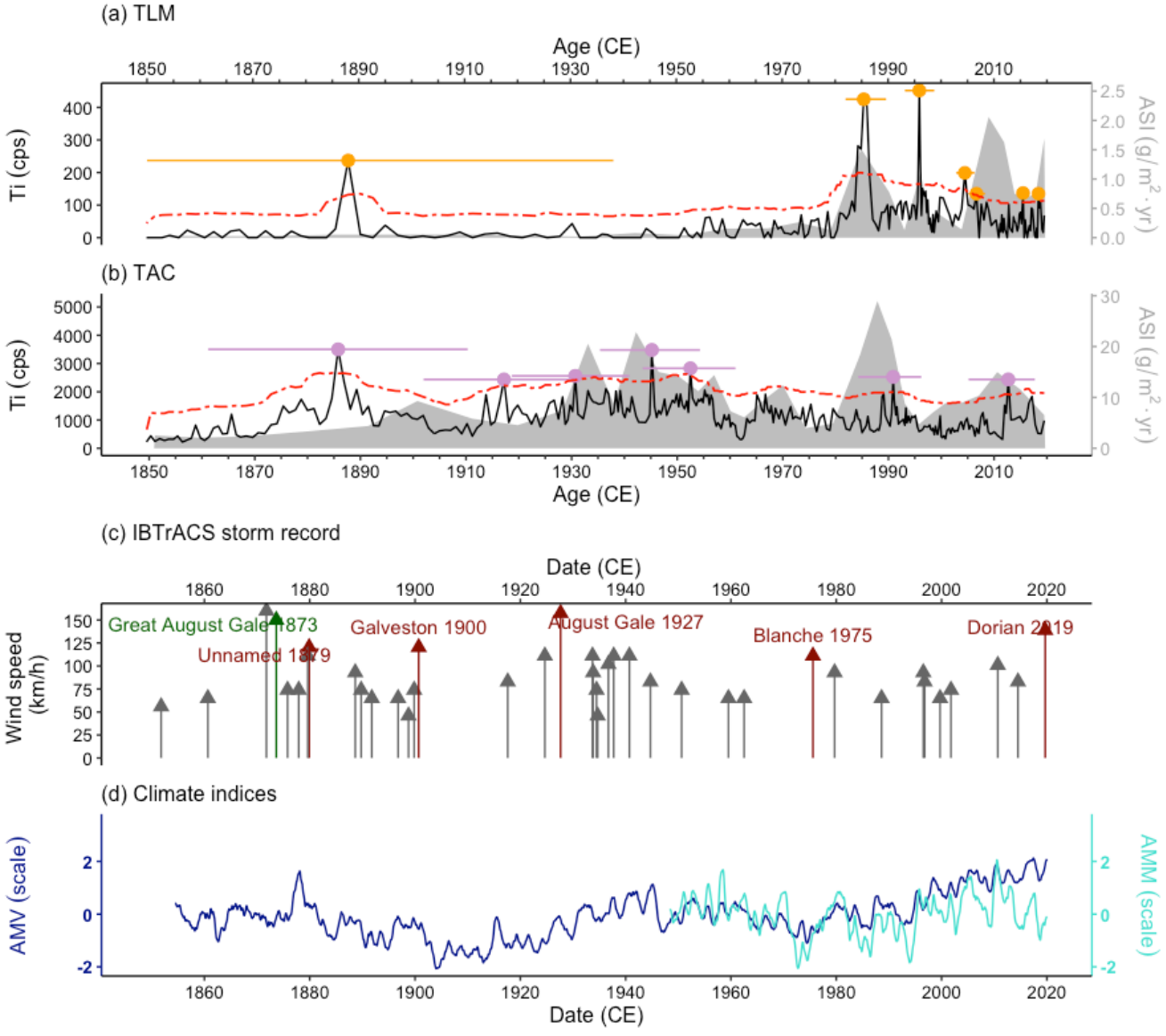


**Figure 7. (a–b) Modern (1851–2019 CE) storm proxies for TLM (a; in orange) and TAC (b; in purple): the Aeolian Sand Index (ASI; g m$^2$ yr$^{-1}$) and Ti measurements (CPS). Dot-dashed red lines indicate the moving thresholds of event detection, calculated using the Tukey rule (see Methods for details). Events are marked by orange (TLM) and purple (TAC) dots, with horizontal bars representing age uncertainty. (c) Bar chart showing historical wind data from the IBTrACKS dataset (Knapp et al., 2010; Gahtan et al., 2024) showing storms passing within 100 km of the Magdalen Islands and their peak winds (km h$^{-1}$). Storms with documented impacts in local newspapers and shipwreck records are highlighted in red. The Great August Gale of 1873, highlighted in green, was not in the IBTrACS dataset, but had known impacts on the Magdalen Islands. (d) Instrumental time-series of the Atlantic Meridional Mode (AMM; turquoise) from 1948–2023 (Chiang and Vimont, 2004) and of the Atlantic Multidecadal Variability (AMV; in dark blue) from 1854-2023 (Huang et al., 2017).**

https://doi.org/10.5194/egusphere-2025-400
Preprint. Discussion started: 19 February 2025


### 5.3 Western North Atlantic Basin comparison

The TLM and TAC records together offer a 4000-year chronology of storm activity for the Magdalen Islands, adding critical insights to the limited records available from the northern extent of the North Atlantic hurricane track. Despite being aeolian reconstructions, the Magdalen Islands records show notable similarity with marine overwash records from lakes and blue holes spanning the past 2000 years from eastern Canada, the US, and the Bahamas (Fig. 8). This north-south transect across the western North Atlantic reflects modern storm tracks from the Magdalen Islands (Fig. 6a) and enable broader regional comparisons.

During the instrumental period (1851 CE–present), the storm records from the Bahamas to the Magdalen Islands show significant heterogeneity (Fig. 8). TLM and TAC documented increased storm activity, particularly in the 20$^{th}$ century (Figs. 8a–b). The only temporally overlapping record from eastern Canada, at Harvey Lake, New Brunswick, also indicates elevated storms activity after ~1895 CE (Patterson et al., 2022). While the Harvey Lake study does not calculate events per century and is thus excluded from Fig. 8, it corroborates trends in TLM and TAC. In contrast, the record from Salt Pond, Massachusetts, does not show a comparable increase (Donnelly et al., 2015) (Fig. 8d), though a nearby record from Mattapoisett Marsh, just 18 km south of Salt Pond, documents numerous 20$^{th}$ century hurricanes strikes (Boldt et al., 2010). Donnelly et al. (2015) attribute this discrepancy to Salt Pond's avoidance of several modern hurricanes. Similarly, the Bahamian compilation, aggregating five blue hole storm records across the archipelago, shows a quiet 20$^{th}$ century (Fig. 8e). This trend reflects mostly inactivity at the southern sites (South Andros, Long Island, and Middle Caicos), while northern sites (Grand Bahamas and Abaco) exhibit increased storm activity (Wallace et al., 2021a; Winkler et al., 2023).

The Little Ice Age (LIA), which lasted between ~1300–1850 CE in the Gulf of St. Lawrence (Magnan and Garneau, 2014) stands out as an active period across the western North Atlantic. At TLM, increased storm activity persisted between 1220–1785 CE, interrupted only by a calm interval between 1320–1390 CE (Fig. 8a). Similarly, TAC shows heightened activity 1315–1710 CE, with a calm period between 1400–1435 CE, and a peak between 1500–1700 CE (Fig. 8b). These trends align with Robinson Lake, Nova-Scotia, which shows increased storm activity between 1475–1670 CE (Oliva et al., 2018) (Fig. 8c), and Harvey Lake, New Brunswick, where coarse silt beds were deposited between 1630–1640 CE (Patterson et al., 2022). Salt Pond also experienced elevated storm activity with 35 events between 1500–1600 CE (Donnelly et al., 2015) (Fig. 8d). In the Bahamas, storm activity peaked between 1570–1670 CE (Fig. 8e), matching patterns observed in the Magdalen Islands and nearby sites (Winkler et al., 2023). Notably, none of these records document storm activity during the early LIA (~1200–1400 CE), as seen in the Magdalen Islands.

During the Medieval Climate Anomaly (MCA), which lasted between ~ 900–1300 CE in the Gulf of St. Lawrence (Magnan and Garneau, 2014) storm activity decreased across the Magdalen Islands, consistent with calmer periods at Salt Pond and in the Bahamas (Fig. 8d–e). However, brief upticks between 1000–1100 CE at Salt Pond and 980–1030 CE in the Bahamas contrast with calm conditions in the Magdalen Islands. In the Bahamas, the increase is attributed to southern sites like Southern Andros (Wallace et al., 2019) and Middle Caicos (Wallace et al., 2021a), while northern sites, such as the Grand

https://doi.org/10.5194/egusphere-2025-400
Preprint. Discussion started: 19 February 2025


Bahamas, recorded a decrease in storm frequency from 550–1090 CE (Winkler et al., 2023) (see Fig. 6a for location). Between 600–800 CE, sediment delivery at TLM and TAC aligns with increased storm activity in the Bahamas (720–820 CE), while Salt Pond documented an earlier active period between 300–600 CE, partly overlapping with elevated sediment delivery at TAC (Fig. 8c). Unfortunately, the lack of pre-LIA eastern Canadian records limits our understanding of storm dynamics earlier in the record, while the shorter duration of the Salt Pond and Bahamas reconstructions (<2000 years) restricts longer-term comparison with the Magdalen Islands data.

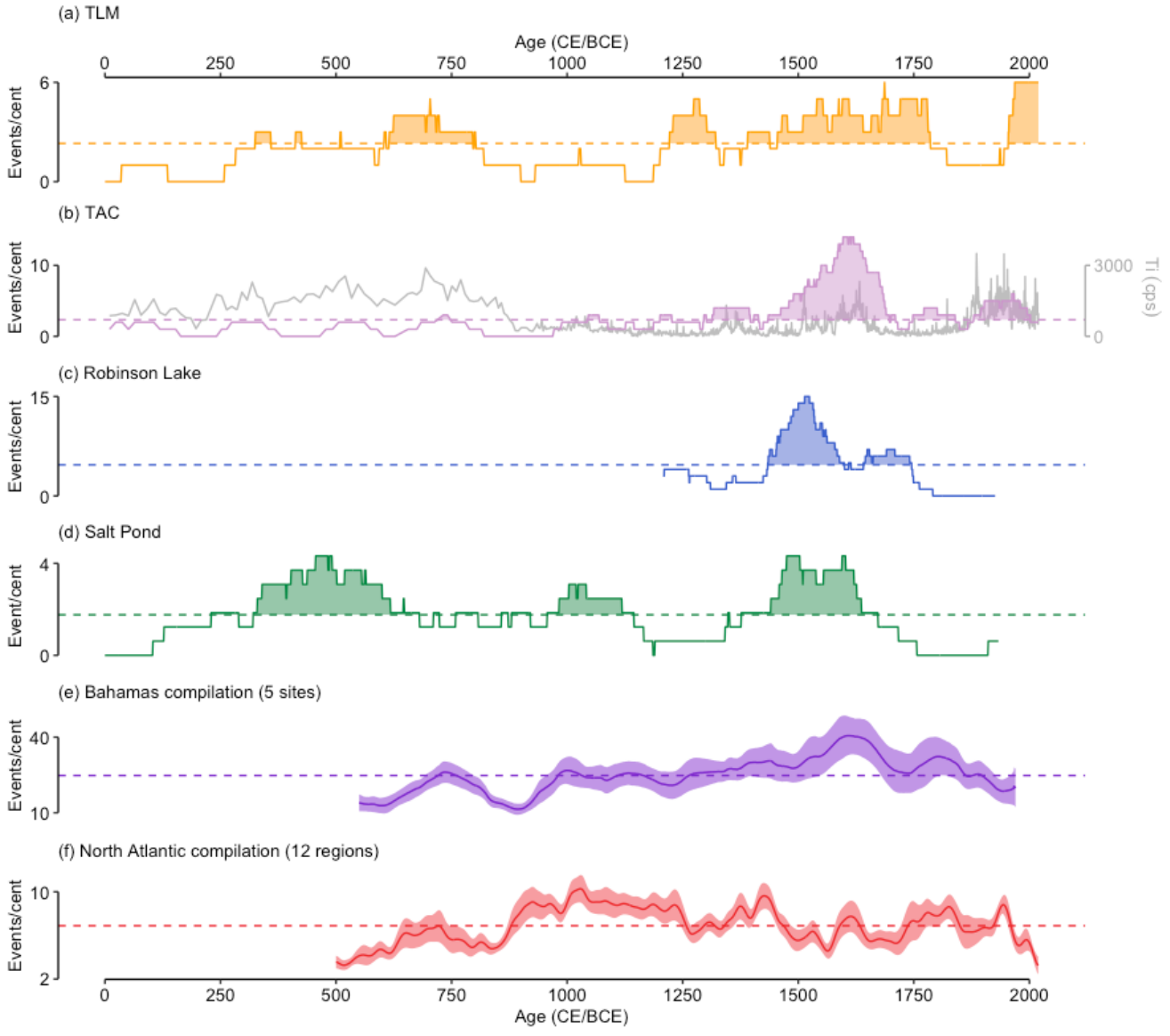


**Figure 8. Events per century (Event/cent) from the Magdalen Islands and nearby regions reconstructions. (a–b) 100-year moving sum of storm events at TLM (orange line) and TAC (purple line). The grey line in (b) presents the Ti data from TAC, emphasizing**

https://doi.org/10.5194/egusphere-2025-400
Preprint. Discussion started: 19 February 2025


**its similarity to the storm activity pattern from TLM (a). (c–e) Comparisons with previously published paleo-storm reconstructions. c) 100-year moving sum of storm overwash events from Robinson Lake, Nova Scotia, between 1210–1925 CE (Oliva et al., 2017). (d) 100-year moving sum of storm overwash events from Salt Pond, Massachusetts, spanning the past 2000 years (Donnelly et al., 2015). (e) A smoothed 1500-year compilation of storm records from five Bahamian blue hole records, with the shaded area representing the confidence interval (Wallace et al., 2019; Winkler et al., 2020; Wallace et al., 2021a; Wallace et al., 2021b; Winkler et al., 2023). Compilation methods are detailed in Wallace et al. (2021a). The location of the studies in a–e is shown in Fig. 6a. (f) Smoothed 1500-year compilation of storm records from 12 regions spanning from Belize to New England from Yang et al. (2024).**

### 5.4 Long-term climate drivers of storm activity

Storm records from the Magdalen Islands, eastern Canada, New England, and the Bahamas reveal consistent patterns suggesting that our Magdalen Islands records capture storms originating in the Main Development Region (MDR), located in the tropical Atlantic off West Africa. These storms typically track through the Bahamas before recurving towards the US east coast and eastern Canada, a pattern consistent with the IBTrACS storm tracks observed in the Magdalen Islands since 1851 CE (Fig. 5a).

Hurricane activity in the MDR is strongly influenced by the Atlantic Meridional Mode (AMM), a coupled ocean-atmosphere system driven by variations in tropical Atlantic sea surface temperatures (SSTs) and vertical wind shear (VWS) (Kossin and Vimont, 2007; Vimont and Kossin, 2007; Klotzbach and Gray, 2008; Kossin, 2017; Ting et al., 2019). Positive AMM phases, characterized by elevated SSTs and reduced VWS, creates favourable conditions for storm formation and intensification (Kossin, 2017). While long-term AMM reconstructions are currently unavailable, its correlation to the Atlantic Multidecadal Variability (AMV), a basin-wide pattern of decadal Atlantic SSTs fluctuation, provides an indirect mean of assessing long-term hurricane trends. The instrumental AMV record correlates positively with instrumental AMM data (Fig. 7d), and the AMV has been extensively reconstructed using proxies (e.g., Fig. 5c). Variations in AMV are though to modulate long-term hurricane activity indirectly by exciting trends in AMM (Kossin and Vimont, 2007; Vimont and Kossin, 2007). The annually resolved AMV reconstruction from Lapointe et al. (2020), based on a varved lake in the Canadian Arctic, identifies a strong negative AMV during the LIA (not conducive to hurricane formation) and a more positive phase during the MCA (conducive to hurricane formation) (Fig. 5c). This trend is corroborated by other coarser-resolution AMV reconstructions (Mann et al., 2009b; Wang et al., 2017).

Nevertheless, storm records from eastern Canada (including our own from the Magdalen Islands), New England, and the Bahamas show widespread agreement regarding heightened activity during the LIA, and moderate consensus on reduced activity during the MCA, which is contrary to what would be expected based on the AMV record. For instance, Mann et al. (2009a), in a statistical reconstruction of paleo-hurricane frequency across the North Atlantic, estimated low hurricane counts during the LIA and higher counts during the MCA. Additionally, a recent synthesis of proxy-based paleo-storm reconstructions spanning 12 regions from Belize to New England (Yang et al., 2024) supports the results from Mann et al. (2009a), showing elevated storm frequency from 900–1200 CE, following by a calm period from 1250–1700 CE, interrupted only by a peak in activity between 1375–1475 CE (Fig. 8f).

https://doi.org/10.5194/egusphere-2025-400
Preprint. Discussion started: 19 February 2025


Interestingly, the Yang et al. (2024) compilation contrasts markedly with our records, as well as others from eastern Canada, New England, and the Bahamas. This persistent antiphase pattern, alongside a negative correlation to the AMV (which typically promotes hurricane formation), suggests that during periods of suppressed hurricane activity in the North Atlantic – such as the LIA – local factors steered the fewer storms that formed towards the northern Bahamas, the US east coast, and eastern Canada. Our findings indicate that storm frequency in these regions is influenced less by factors driving storm genesis in the tropical Atlantic (e.g., AMM and AMV), and more by processes that either intensify storms locally or shift storm tracks towards higher latitudes. For example, Patterson et al. (2022) and Oliva et al. (2018) proposed that elevated storm activity during the early LIA might reflect local warmer SSTs in the Gulf of Maine and the Sargasso Sea, despite cooler temperatures in the MDR. Dickie and Wach (2024) provide a concise summary of these mechanisms, highlighting that while the LIA experienced colder winter and lower annual mean temperatures, warmer summers may have been sufficient to fuel local storm intensification in mid-latitudes North America.

Supporting this hypothesis, Ting et al. (2019) identified a dipole pattern over the last 150 years, where favourable hurricane formation conditions in the MDR (positive AMV: higher SSTs, reduced VWS) coincide with unfavourable conditions along the US east coast (cooler SSTs, higher VWS), and vice versa. If this dipole operated during the LIA, regional conditions along the US east coast may have intensified hurricanes locally, while during the MCA, higher overall hurricane activity likely directed more storms towards the Gulf of Mexico and Caribbean. Indeed, a 1700 year-long western Florida compilation shows frequent storms between 750–1300 CE and lower activity between 1300–1800 CE (Wallace et al., 2021a; Winkler et al., 2023). This antiphase pattern seems to persist over the long-term with the Magdalen Islands records: a 5500-year record from Mullet Pond, in the Florida panhandle, indicates active periods between 150-350 CE, 150-1 BCE, 550-400 BCE and 950-800 BCE (Wang et al., 2024), which all correspond to quiet intervals at the Magdalen Islands (Fig. 5).

Finally, another key factor influencing hurricane tracks is the position and strength of the North Atlantic subtropical high, also known as the Bermuda High. Modern observations show that a strengthened and westward-expanding Bermuda High drives hurricanes towards the Gulf of Mexico, while a weaker, eastward-shifted Bermuda High favours recurving tracks towards the US east coast (Kossin et al., 2010; Colbert and Soden, 2012). However, the absence of long-term reconstructions of Bermuda High dynamics limits our ability to analyse its influence over centennial to millennial timescales, as highlighted in several studies (Wallace et al., 2021b; Bregy et al., 2022).

## 6. Conclusion

The Magdalen Islands, located near the centre of the Gulf of St. Lawrence, have been impacted by post-tropical cyclones and other storm events over the last century, and our results provide important new data on paleo-storm history from one of the most northern sites studied for these events in the western North Atlantic, and one which is highly sensitive to ongoing climate warming.

https://doi.org/10.5194/egusphere-2025-400
Preprint. Discussion started: 19 February 2025


Our 4000-year aeolian-based storm chronology from the Magdalen Islands demonstrates the viability of peatlands for such studies and offers critical insights into storm dynamics at the northern limit of the North Atlantic hurricane track. Furthermore, the comparability of our findings with existing North American paleo-storm records — primarily derived from marine and coastal overwash deposits — demonstrates the complementary value of aeolian and peatland records. These archives can enrich the paleo-storm literature in North America and provide a broader perspective on past storm activity.

One challenging task that emerged from our results is a proper calibration of peat-based proxies to the historical storm records. While our data show some correspondence with IBTrACS records over the past 150 years, identifying specific storms remains difficult. Future studies should prioritize the development of high-resolution age-models from undisturbed surface peat cores to refine calibration methods and better understand contemporary relationships between storm and sediment deposition in peatlands, supporting the interpretation of peat-based storm records.

Our results also highlight the specific challenges of working with peat records. Despite their proximity, our two study sites exhibited critical differences that were essential to address for an accurate storm record interpretation. For instance, differences in the amount and composition of sediments between the TLM and TAC storm records were linked to variations in bog size and distance from sediment sources, which influenced the strength of the storm signals. TAC displayed a stronger signal, sensitive to long-term environmental and climatic changes, whereas TLM's signal was more muted but exhibited greater consistency over time. These findings underscore the importance of considering such factors when selecting sites for future research.

Finally, our data reinforce the existence of an antiphase pattern in storms records between the Gulf of Mexico and the Caribbeans versus those north of the Bahamas. This finding extends the hypothesis that storm records north of the Bahamas may be in antiphase with basin-wide records from the North Atlantic. Future studies should investigate climatic mechanisms driving this antiphase pattern, as understanding these processes will prove important to estimate future storm impacts in eastern Canada.

## Data availability

All raw data can be provided by the corresponding author upon request. Paleo-storm reconstruction data will also be available on the *Borealis* data repository (https://borealisdata.ca/) upon publication.

## Author contributions

AL, MP, and JSJ planned the study fieldwork campaign and conceptualization. AL designed the methodology, conducted the investigation, analysed the data, and wrote and prepared the original draft (writing and visualization). PF supervised µ-XRF data acquisition and supported data analysis. NKS supervised $^{210}$Pb dating data acquisition and supported data analysis and age-depth modelling. AL, MP, JSJ, PF, and NKS reviewed and edited the draft. MP and JSJ supervised all steps of the research.

https://doi.org/10.5194/egusphere-2025-400
Preprint. Discussion started: 19 February 2025


## Competing interests

The authors have the following competing interests: At least one of the (co-)authors is a member of the editorial board of Climate of the Past. Dr. Pierre Francus is a member of the editorial board of Climate of the Past.

## Acknowledgements

We thank Sydney Moser and Tania O'Reilly for their assistance during the 2020 fieldwork campaign on the Magdalen Islands; Michelle Garneau and Leonie Perrier (GEOTOP – UQAM) for their valuable guidance in peat stratigraphy analysis; Arnaud De Coninck (INRS) for conducting the µ-XRF analysis and providing analytical support; and Steve Pratte (Zhejiang University) and Pascale Biron (Concordia University) for their insightful reviews of the master's thesis chapter upon which this paper is based.

https://doi.org/10.5194/egusphere-2025-400
Preprint. Discussion started: 19 February 2025


## Appendix A: Wind rose from the Magdalen Islands

**Figure A1. Seasonal wind roses displaying the 12 directions of incoming winds based on daily peak wind gusts data from 1984 to 2018 on the Magdalen Islands. The number of days (expressed as %) for any category of speed of peak wind gusts (in km $h^{-1}$) are indicated for each wind direction.**

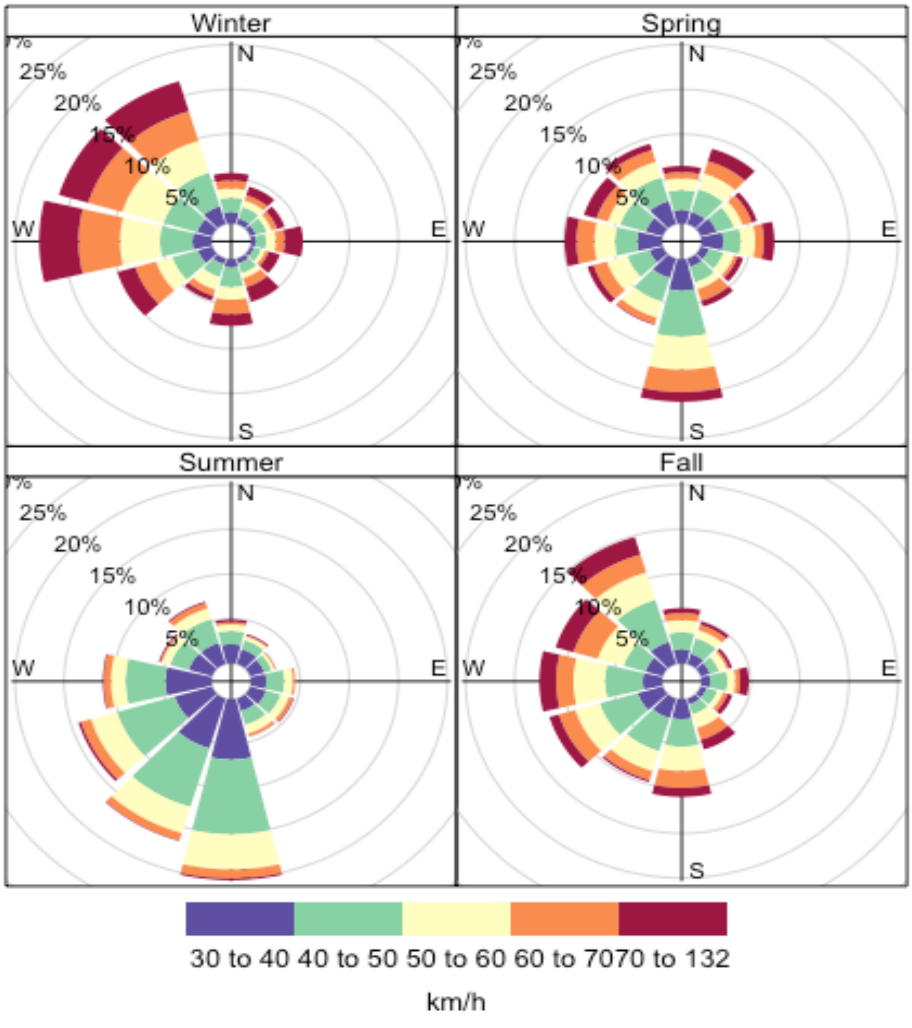

https://doi.org/10.5194/egusphere-2025-400
Preprint. Discussion started: 19 February 2025


## Appendix B: Construction of the two composite cores

**Table B1. Main cores drives from the TLM and TAC sites. The TLM composite core consists of the first 25 cm of TLM-monolith (0–25 cm), the first 75 cm of TLM-2 (25–100 cm) and the entire TLM-1 drive (100–700 cm). The TAC composite core consists of the first 25 cm of TAC-monolith (0-25 cm), the entire TAC-2 drive (25–275 cm), and a 50 cm segment from TAC-3 (275–325 cm). The remaining portion of TLM-2 and the entire TAC-1 core were archived for possible future analyses.**

| Core drive name | Actual depth (cm) | Portion used in composite core (cm) |
|---|---|---|
| *TLM* | | |
| TLM-monolith | 0–50 | 0–25 |
| TLM-1 | 100–700 | 100–700 |
| TLM-2 | 25–675 | 25–100 |
| *TAC* | | |
| TAC-monolith | 0–50 | 0–50 |
| TAC-1 | 0–315 | None |
| TAC-2 | 25–275 | 50–275 |
| TAC-3 | 275–325 | 275–325 |

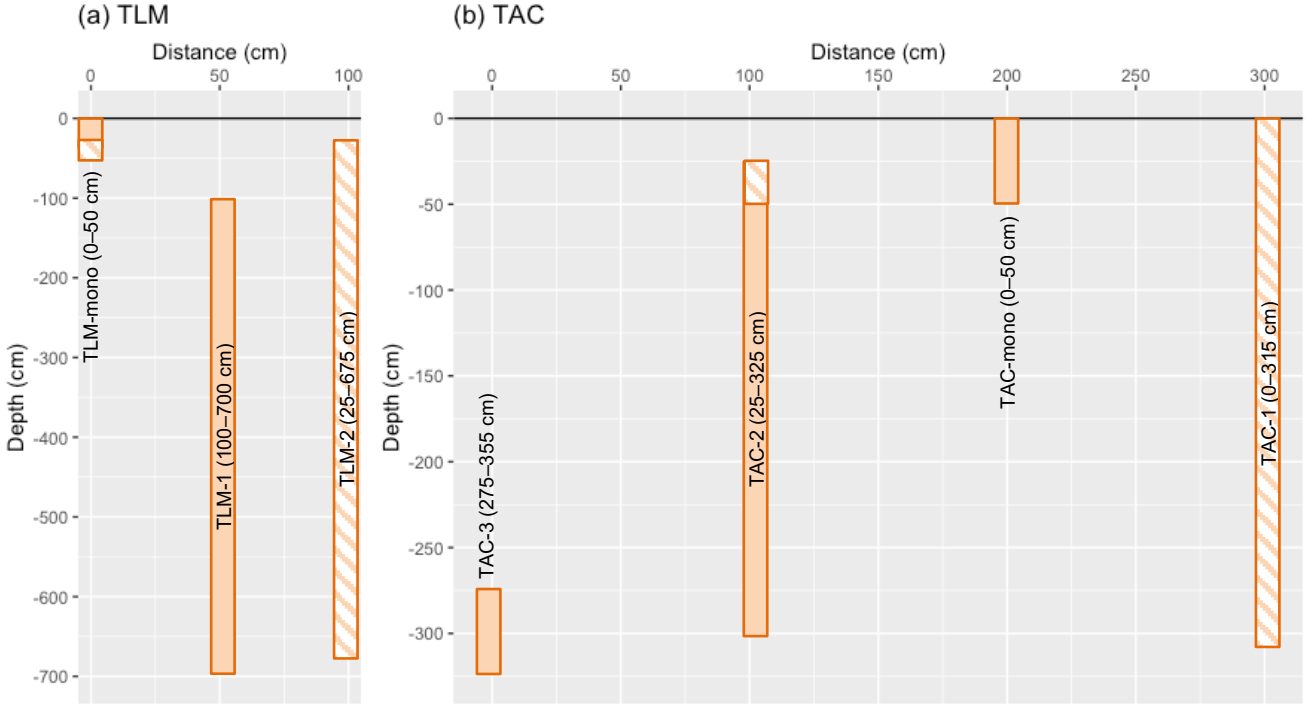


**Figure B1. Depth diagrams of core drives for TLM (a) and TAC (b). Note that the *y*-axis scales differ between the two panels. Solid orange rectangles represent core drives and segments used to construct the composite cores. Hatched orange rectangles indicate core drives and segments reserved for preliminary analyses, other research, or reference purposes. (a) The TLM composite core includes: the segment from the surface to 25 cm (TLM-monolith); 25 cm to 100 cm (TLM-2); and the entire TLM-1 core. (b) The TAC composite core includes: the full 50 cm length of TAC-monolith; 50 cm to 275 cm (TAC-2); and the full 50 cm length of TAC-3.**

https://doi.org/10.5194/egusphere-2025-400
Preprint. Discussion started: 19 February 2025


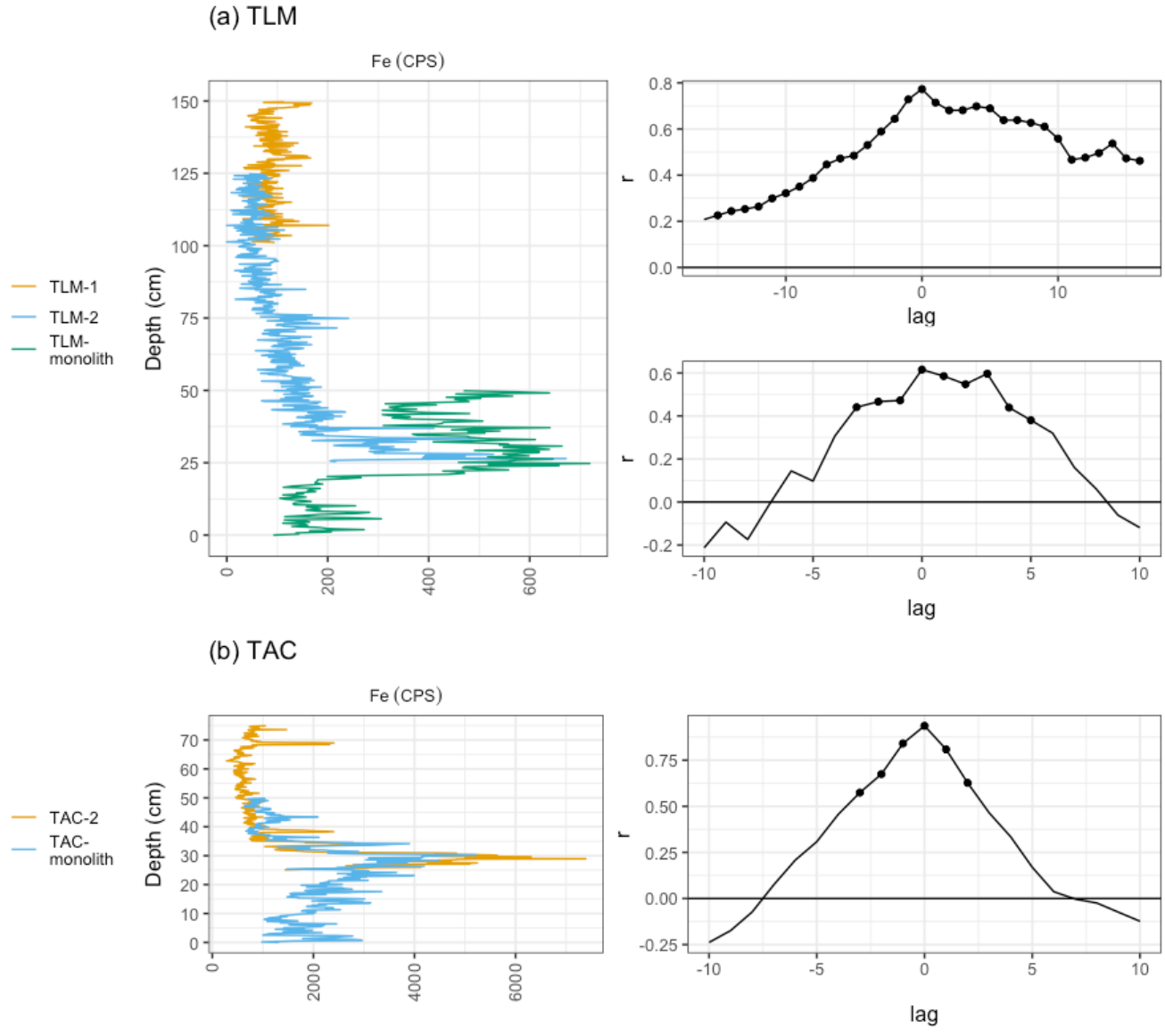


**Figure B2. Core drive alignment confirmed through cross-correlation analysis (CCA) of overlapping Fe µ-XRF measurements. Iron was used due to its abundance and consistent patterns across core drives. Black dots in the right-hand side CCA diagrams indicate significance ($p < 0.05$). (a) In the TLM composite core, cross-correlations between TLM-1 and TLM-2 (100–125 cm) and between TLM-2 and TLM-monolith (25–49 cm) showed strong positive correlation coefficient ($r = 0.8$ and $r = 0.6$, $p < 0.05$, at lag = 0), respectively, confirming alignment. (b) In the TAC composite core, TAC-2 and TAC-monolith's cross-correlation between 25–49 cm showed a strong positive correlation coefficient at lag = 0 ($r = 0.9$, $p < 0.05$), confirming alignment.**

https://doi.org/10.5194/egusphere-2025-400
Preprint. Discussion started: 19 February 2025


## Appendix C: Chronostratigraphy

**Table C1. Accelerator mass spectrometry (AMS) radiocarbon ($^{14}$C) results for TLM and TAC. Dated material includes bulk peat sediment (bulk) and wood fragments (wood). Uncalibrated $^{14}$C dates are shown as years before 1950 (BP). The $^{14}$C dates were processed using the Bayesian *rplum* algorithm in R and calibrated with the IntCal20 curve. Calibrated dates are presented as both calibrated years before 1950 (cal. BP) and as Common Era/Before Common Era (CE/BCE).**

| Sample depth (cm) | Lab ID | Material | AMS $^{14}$C age BP (uncal.) | Calibrated 2 sigma range | | Mean modelled age (uncertainty) (CE/BCE) |
|---|---|---|---|---|---|---|
| | | | | Cal. BP | CE/BCE | |
| ***TLM*** | | | | | | |
| 59-60 | UOC-18434 | Bulk | 174 ± 21 | 289 – 73 | 1661 – 1916 CE | 1825 (1750 – 1890) CE |
| 122-123 | UOC-14324 | Wood | 417 ± 36 | 526 – 327 | 1425 – 1624 CE | 1455 (1350 – 1510) CE |
| 243-244 | UOC-15799 | Wood | 1582 ± 35 | 1532 – 1390 | 418 – 561 CE | 495 (415 – 585) CE |
| 390-391 | UOC-15800 | Wood | 2491 ± 26 | 2723 – 2469 | 774 – 520 BCE | 605 (745 – 470) BCE |
| 484-485 | UOC-15801 | Wood | 3014 ± 28 | 3335 – 3078 | 1386 – 1129 BCE | 1270 (1380 – 1150) BCE |
| 577-578 | UOC-14325 | Wood | 3572 ± 37 | 3978 – 3724 | 2029 – 1775 BCE | 1930 (2030 – 1805) BCE |
| 634-635 | UOC-15802 | Wood | 3813 ± 26 | 4346 – 4093 | 2397 – 2144 BCE | 2365 (2490 – 2230) BCE |
| 669-670* | UOC-18285 | Wood | 7923 ± 19 | 8979 – 8604 | 7030 – 6655 BCE | 2730 (3015 – 2515) BCE |
| 674-675* | UOC-14326 | Wood | 7650 ± 32 | 8536 – 8382 | 6581 – 6433 BCE | 2780 (3080 – 2250) BCE |
| ***TAC*** | | | | | | |
| 31-32 | UOC-18435 | Bulk | 6 ± 21 | 249 – 41 | 1701 – 1909 CE | 1940 (1930 – 1950) CE |
| 57-58 | UOC-15803 | Wood | 162 ± 26 | 287 – 43 | 1664 – 1908 CE | 1730 (1670 – 1785) CE |
| 76-77 | UOC-18286 | Wood | 341 ± 13 | 469 –316 | 1482 – 1635 CE | 1565 (1495 – 1625) CE |
| 102-103 | UCO-18436 | Bulk | 613 ± 20 | 649 – 551 | 1301 – 1400 CE | 1340 (1300 – 1395) CE |
| 122-123 | UOC-15804 | Wood | 869 ± 26 | 900 – 693 | 1050 – 1257 CE | 1150 (1060 – 1210) CE |
| 128-129 | UOC-18287 | Wood | 964 ± 14 | 921 – 797 | 1030 – 1154 CE | 1070 (970 – 1140) CE |
| 133-134 | UCO-18437 | Bulk | 992 ± 21 | 957 – 798 | 994 – 1153 CE | 945 (775 – 1040) CE |
| 147-148 | UOC-15805 | Wood | 2469 ± 27 | 2712 – 2371 | 763 – 422 BCE | 475 (630 – 395) BCE |
| 162-163 | UOC-18288 | Wood | 2928 ± 14 | 3159 – 3001 | 1210 – 1052 BCE | 970 (1080 –840) BCE |
| 185-186 | UOC-18438 | Bulk | 3052 ± 21 | 3350 – 3178 | 1401 – 1229 BCE | 1260 (1350 – 1145) BCE |
| 199-200 | UOC-15806 | Wood | 3178 ± 27 | 3452 – 3361 | 1503 – 1412 BCE | 1400 (1470 – 1305) BCE |
| 226-227 | UOC-15807 | Wood | 3300 ± 28 | 3571 – 3455 | 1622 – 1506 BCE | 1600 (1690 – 1525) BCE |
| 258-259 | UOC-15808 | Wood | 3508 ± 29 | 3870 – 3694 | 1921 – 1745 BCE | 1885 (2005 – 1800) BCE |
| 283-284 | UOC-15809 | Wood | 3597 ± 28 | 3980 – 3834 | 2031 – 1885 BCE | 2155 (2295 –2035) BCE |
| 296-297 | UOC-15810 | Wood | 3771 ± 30 | 4240 – 3996 | 2291 – 2047 BCE | 2370 (2490 – 2240) BCE |
| 319-320 | UOC-18289 | wood | 4376 ± 17 | 5025 – 4865 | 3076 – 2916 BCE | 2960 (3065 – 2915) BCE |

*** The AMS $^{14}$C dates at these depths were inverted and were considered outliers by the *rplum* R algorithm. Therefore, the modelled mean dates associated with these depths do not reflect the AMS $^{14}$C date.**

https://doi.org/10.5194/egusphere-2025-400
Preprint. Discussion started: 19 February 2025


**Table C2. Total $^{210}$Pb activity results for TLM and TAC measured at the GEOTOP Radiochronology Laboratory at the *Université du Québec à Montréal* (UQAM). The background $^{210}$Pb level for TLM was taken from the background $^{210}$Pb level at TAC (17.5 Bq kg$^{-1}$)**

| Sample depth (cm) | Lab ID | Dry Density (g cm$^{-3}$) | $^{210}$Pb (Bq kg$^{-1}$) | Mean modelled age (uncertainty) (CE) |
|---|---|---|---|---|
| ***TLM*** | | | | |
| 3.6 | 11366 | 0.04 | 300.67 ± 22.61 | 2018 (2017 – 2018) |
| 7.1 | 11367 | 0.04 | 331.2 ± 24.12 | 2016 (2015 – 2017) |
| 10.7 | 11368 | 0.04 | 335.54 ± 24.4 | 2014 (2013 – 2015) |
| 14.3 | 11369 | 0.04 | 261.04 ± 19.6 | 2012 (2011 – 2013) |
| 17.9 | 11370 | 0.05 | 494.38 ± 35.6 | 2009 (2008 – 2010) |
| 21.4 | 11371 | 0.06 | 405.92 ± 28.81 | 2004 (2002 – 2006) |
| 25 | 11372 | 0.06 | 325.84 ± 24.3 | 1999 (1997 – 2001) |
| 28.6 | 11373 | 0.05 | 274.68 ± 20.79 | 1995 (1992 – 1999) |
| 32.1 | 11374 | 0.06 | 310.76 ± 22.45 | 1989 (1986 – 1993) |
| 35.7 | 11375 | 0.06 | 383.36 ± 26.56 | 1980 (1976 – 1984) |
| 39.3 | 11376 | 0.06 | 313.56 ± 21.67 | 1968 (1962 –1976) |
| 42.8 | 11377 | 0.07 | 234.26 ± 16.49 | 1956 (1948 – 1967) |
| 46.4 | 11378 | 0.07 | 188.63 ± 13.49 | 1939 (1925 – 1956) |
| 50 | 11379 | 0.07 | 190.79 ± 14.44 | 1907 (1867 – 1942) |
| ***TAC*** | | | | |
| 3.3 | 11342 | 0.09 | 468.19 ± 32.56 | 2009 (2003 – 2014) |
| 6.7 | 11343 | 0.08 | 387.3 ± 26.51 | 2002 (1997 – 2007) |
| 10 | 11344 | 0.06 | 268.28 ± 19.39 | 1997 (1991 – 2002) |
| 13.3 | 11345 | 0.06 | 269.6 ± 19.4 | 1991 (1985 – 1997) |
| 16.7 | 11346 | 0.08 | 219.05 ± 15.61 | 1985 (1979 – 1991) |
| 20 | 11347 | 0.13 | 200.85 ± 13.88 | 1975 (1968 – 1982) |
| 23.3 | 11348 | 0.07 | 171.74 ± 12.1 | 1967 (1960 – 1973) |
| 26.7 | 11349 | 0.08 | 151.57 ± 11.62 | 1957 (1949 – 1965) |
| 30 | 11350 | 0.09 | 124.78 ± 8.56 | 1946 (1937 – 1956) |
| 33.3 | 11351 | 0.11 | 91.24 ± 6.33 | 1932 (1922 – 1942) |
| 36.7 | 11392 | 0.15 | 72.63 ± 4.2 | 1905 (1887 – 1922) |
| 40 | 11352 | 0.14 | 41.44 ± 3.03 | 1868 (1827 – 1904) |
| 43.3 | 11393 | 0.12 | 21.5 ± 2.5 | 1839 (1789 – 1884) |
| 46.7 | 11394 | 0.14 | 18.22 ± 1.98 | 1812 (1751 – 1862) |
| 50 | 11353 | 0.09 | 17.44 ± 1.4 | 1785 (1720 – 1840) |

https://doi.org/10.5194/egusphere-2025-400
Preprint. Discussion started: 19 February 2025


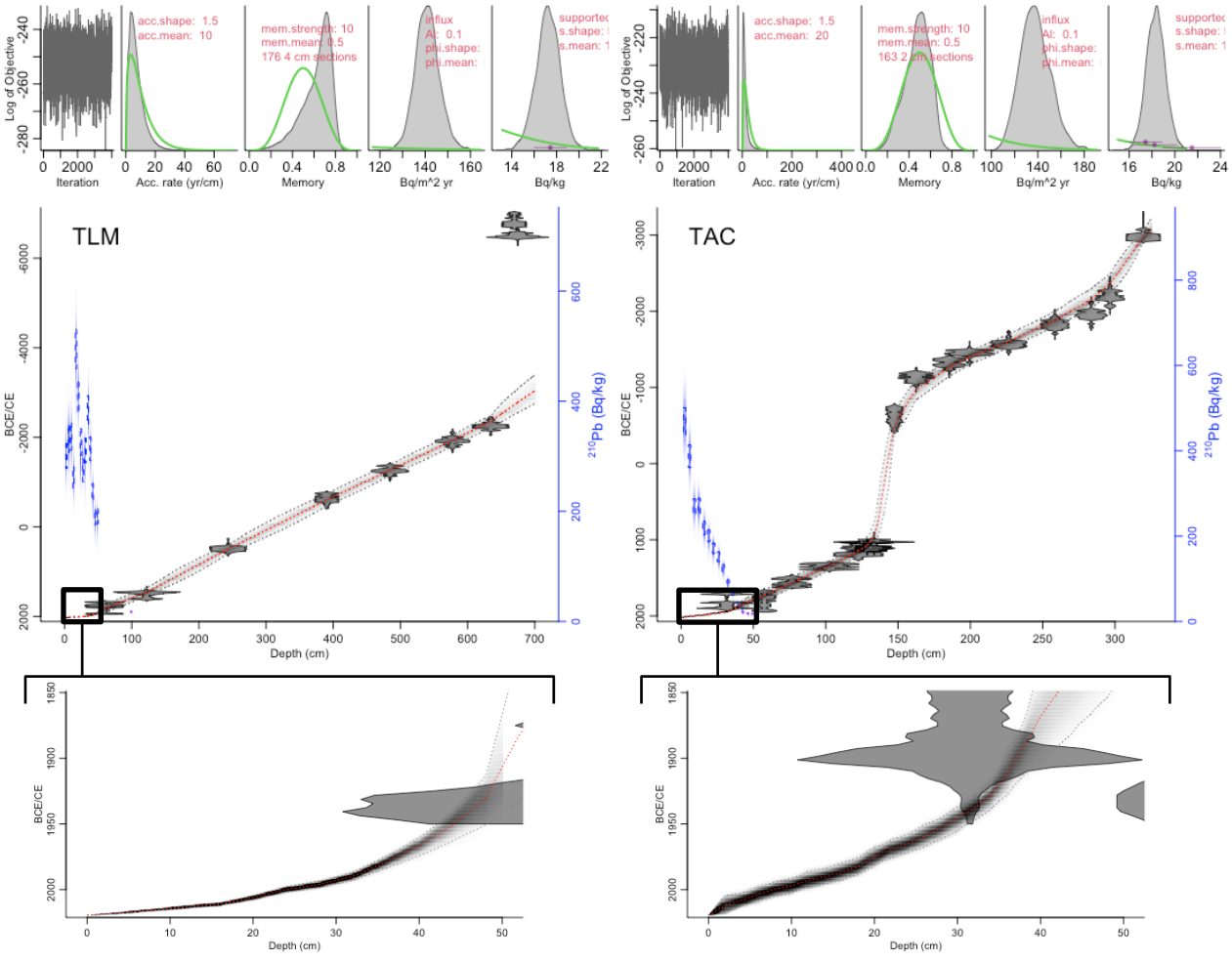


**Figure C1.** ***rplum*-derived age-depth models for TLM (left) and TAC (right). Radiocarbon ($^{14}$C) dates are shown in grey along the mean age model (dotted red). The rate of supported $^{210}$Pb (right axis) is indicated by blue boxes on the left side (the blue boxes are the measured $^{210}$Pb values, while the blue shadings represent the modelled $^{210}$Pb values). For each core, the upper left panel shows the Markov Chain Monte Carlo (MCMC) iterations; followed by the prior (green curve) and posterior (grey histogram) distributions for the accumulation rate (second panel), memory (third panel), $^{210}$Pb influx in Bq m$^{-2}$ yr$^{-1}$ (fourth panel) and supported $^{210}$Pb in Bq kg$^{-1}$ (fifth panel). A homing-in on the first 50 cm of the age-depth models is shown in the bottom panels.**

https://doi.org/10.5194/egusphere-2025-400
Preprint. Discussion started: 19 February 2025


## Appendix D: Core pictures

(a) TLM

| TLM-2 25–75 | TLM-2 75–100 | TLM-1 100–150 | TLM-1 150–200 | TLM-1 200–250 | TLM-1 250–300 | TLM-1 300–350 | TLM-1 350–400 | TLM-1 400–450 | TLM-1 450–500 | TLM-1 500–550 | TLM-1 550–600 | TLM-1 600–650 | TLM-1 650–700 |
|---|---|---|---|---|---|---|---|---|---|---|---|---|---|

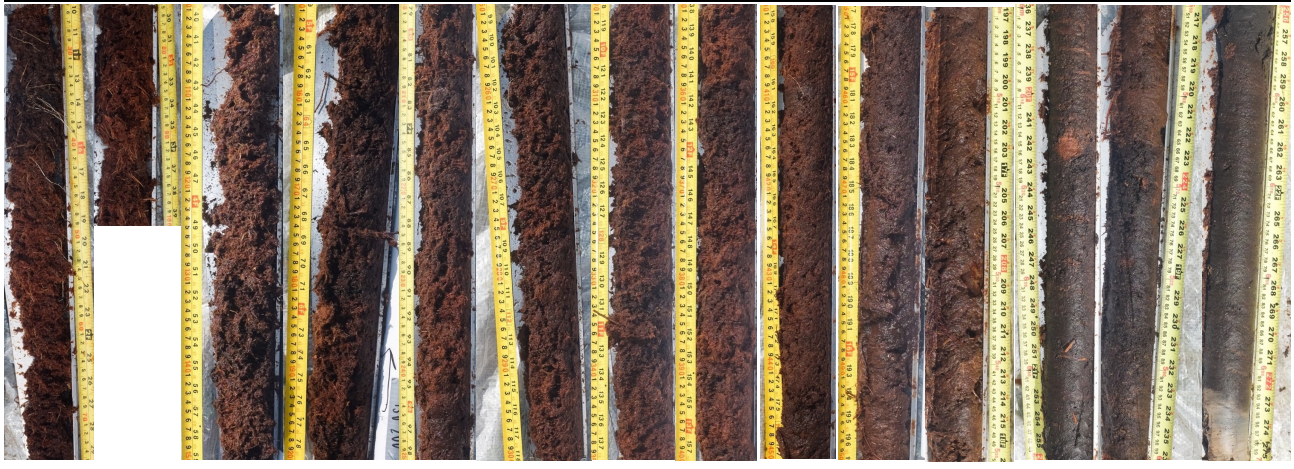

(b) TAC

| TAC-2 25–75 | TAC-2 75–125 | TAC-2 125–175 | TAC-2 175–225 | TAC-2 225–275 | TAC-3 275–325 |
|---|---|---|---|---|---|

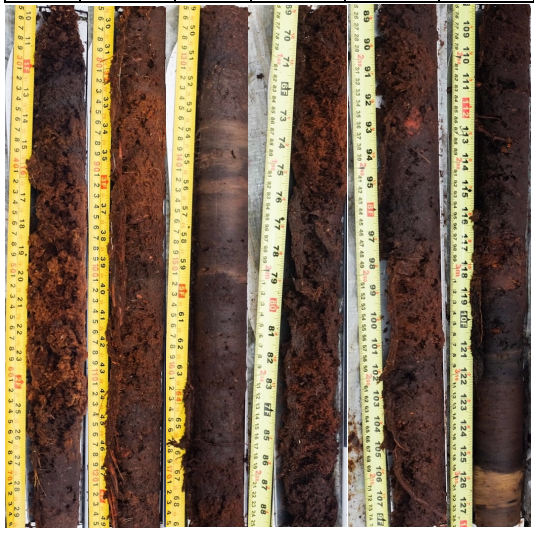

**Figure D1. Photographs of the core segments taken at the TLM (a) and TAC (b) sites after extraction from the peatlands with depth indicated in cm. Only sections included in the TLM and TAC composite core are shown, except for the surface monoliths. (a) The basal sand unit is visible in TLM-1 650–700 between 693–700 cm. (b) The basal sand unit is visible in TAC-3 275–325 cm between 317–325 cm.**

https://doi.org/10.5194/egusphere-2025-400
Preprint. Discussion started: 19 February 2025


## Appendix E: Correlation results

**Table E1. Pearson correlation coefficients among µ-XRF variables (CLR–transformed) and both ASI (log[ASI]) and mineral content (log[minerals/100-minerals), presented for the core stratigraphic zones and upper 50 cm for TLM (a–b) and TAC (c–e; next page). Micro-XRF variables were averaged at 1 cm intervals to match the mineral content and ASI resolution.**

**(a)**

| | Ti | K | Ca | Mn | Fe | S | Si | ASI | Min |
|---|---|---|---|---|---|---|---|---|---|
| **Ti** | | 0.77*** | -0.40*** | -0.89*** | -0.38*** | -0.78*** | -0.42*** | 0.65*** | 0.75*** |
| **K** | 0.00 | | -0.56*** | -0.91*** | -0.34*** | -0.65*** | -0.46*** | 0.54*** | 0.74*** |
| **Ca** | -0.33*** | 0.22* | | 0.47*** | -0.35*** | 0.14 | 0.55*** | -0.44*** | -0.48*** |
| **Mn** | -0.42*** | 0.34*** | 0.77*** | | 0.35*** | 0.71*** | 0.43*** | -0.66*** | -0.83*** |
| **Fe** | -0.22* | -0.62*** | 0.03 | -0.19* | | 0.69*** | -0.53*** | 0.15 | -0.06 |
| **S** | -0.06 | -0.64*** | -0.62*** | -0.77*** | 0.43*** | | -0.13 | -0.41*** | -0.62*** |
| **Si** | -0.42*** | 0.24** | 0.16 | 0.52*** | -0.51*** | -0.49*** | | -0.60*** | -0.52*** |
| **ASI** | 0.21 | -0.05 | 0.04 | -0.30* | 0.37** | 0.21 | -0.62*** | | 0.85*** |
| **Minerals** | 0.14 | -0.28* | -0.02 | -0.49*** | 0.45*** | 0.45*** | -0.63*** | 0.65*** | |

**TLM (Zone 2 452–565 cm)** — **TLM (Zone 1 565–692 cm)**

**(b)**

| | Ti | K | Ca | Mn | Fe | S | Si | ASI | Min |
|---|---|---|---|---|---|---|---|---|---|
| **Ti** | | 0.12* | -0.65*** | -0.40*** | -0.15** | -0.40*** | -0.52*** | 0.38*** | 0.47*** |
| **K** | 0.17 | | -0.02 | -0.18*** | 0.13** | -0.43*** | -0.75*** | 0.56*** | 0.43*** |
| **Ca** | -0.41** | 0.70*** | | 0.32*** | -0.13** | 0.05 | 0.28*** | -0.32*** | -0.50*** |
| **Mn** | -0.58*** | -0.75*** | -0.16 | | 0.07 | -0.31*** | 0.17*** | -0.13* | -0.33*** |
| **Fe** | 0.19 | -0.60*** | -0.70*** | 0.37** | | -0.18*** | -0.25*** | 0.18** | 0.24*** |
| **S** | -0.51*** | -0.49*** | -0.15 | 0.41** | -0.00 | | 0.39*** | -0.30*** | -0.17* |
| **Si** | -0.38** | -0.86*** | -0.56*** | 0.66*** | 0.32* | 0.38** | | -0.65*** | -0.58*** |
| **ASI** | 0.55** | 0.67*** | 0.21 | -0.77*** | -0.34 | -0.34 | -0.62** | | 0.70*** |
| **Minerals** | 0.80*** | 0.17 | -0.42 | -0.58** | 0.11 | -0.22 | -0.24 | 0.65** | |

**TLM (Upper 0–50 cm)** — **TLM (Zone 3 0–450 cm)**

***** p < 0.001; ** p < 0.01; * p < 0.05**

https://doi.org/10.5194/egusphere-2025-400
Preprint. Discussion started: 19 February 2025


**(c)**

| | Ti | K | Ca | Mn | Fe | S | Si | ASI | Min |
|---|---|---|---|---|---|---|---|---|---|
| **Ti** | | 0.82*** | -0.93*** | -0.94*** | -0.87*** | -0.46** | 0.64*** | 0.49*** | 0.66*** |
| **K** | -0.42*** | | -0.85*** | -0.83*** | -0.86*** | -0.64*** | 0.71*** | 0.59*** | 0.67*** |
| **Ca** | -0.90*** | 0.44*** | | 0.97*** | 0.91*** | 0.39* | -0.81*** | -0.57*** | -0.72*** |
| **Mn** | -0.88*** | 0.50*** | 0.96*** | | 0.89*** | 0.37* | -0.78*** | -0.58*** | -0.72*** |
| **Fe** | -0.53*** | 0.09 | 0.52*** | 0.48*** | | 0.42** | -0.79*** | -0.52*** | -0.61*** |
| **S** | -0.12 | -0.27** | -0.12 | -0.18 | -0.31*** | | -0.57*** | -0.42** | -0.48** |
| **Si** | -0.49*** | -0.02 | 0.37*** | 0.35*** | 0.32*** | -0.31*** | | 0.61*** | 0.69*** |
| **ASI** | 0.06 | 0.02 | -0.05 | -0.02 | 0.04 | -0.04 | -0.10 | | 0.88*** |
| **Minerals** | 0.40*** | -0.09 | -0.48*** | -0.44*** | -0.10 | 0.04 | -0.27** | 0.57*** | |

**TAC (Zone 1 274–316 cm)**

**TAC (Zone 2 159–274 cm)**

**D**

| | Ti | K | Ca | Mn | Fe | S | Si | ASI | Min |
|---|---|---|---|---|---|---|---|---|---|
| **Ti** | | 0.95*** | -0.96*** | -0.92*** | -0.79*** | -0.93*** | 0.95*** | 0.29 | 0.61** |
| **K** | 0.87*** | | -0.92*** | -0.91*** | -0.70*** | -0.98*** | 0.96*** | 0.42* | 0.69*** |
| **Ca** | -0.89*** | -0.78*** | | 0.94*** | 0.77*** | 0.87*** | -0.93*** | -0.26 | -0.53** |
| **Mn** | -0.79*** | -0.87*** | 0.77*** | | 0.73*** | 0.84*** | -0.93*** | -0.38 | -0.61** |
| **Fe** | 0.19* | 0.25** | -0.18* | -0.14 | | 0.62** | -0.76*** | -0.14 | -0.47* |
| **S** | -0.61*** | -0.74*** | 0.45*** | 0.47*** | -0.67*** | | -0.95*** | -0.43* | -0.70*** |
| **Si** | 0.59*** | 0.75*** | -0.60*** | -0.74*** | 0.20* | -0.69*** | | 0.41* | 0.67*** |
| **ASI** | 0.68*** | 0.75*** | -0.65*** | -0.65*** | 0.36*** | -0.64*** | 0.60*** | | 0.83*** |
| **Minerals** | 0.83*** | 0.78*** | -0.76*** | -0.63*** | 0.17 | -0.58*** | 0.53*** | 0.78*** | |

**TAC (Zone 3 135–159 cm)**

**TAC (Zone 4 0–135 cm)**

**E**

| | Ti | K | Ca | Mn | Fe | S | Si | ASI | Min |
|---|---|---|---|---|---|---|---|---|---|
| **Ti** | | 0.76*** | -0.87*** | -0.49*** | 0.46*** | -0.75*** | 0.63*** | 0.74*** | 0.81*** |
| **K** | | | -0.52*** | -0.82*** | 0.37** | -0.81*** | 0.85*** | 0.88*** | 0.69*** |
| **Ca** | | | | 0.30* | -0.41** | 0.50*** | -0.43** | -0.54*** | -0.72*** |
| **Mn** | | | | | -0.05 | 0.48*** | -0.87*** | -0.71*** | -0.40** |
| **Fe** | | | | | | -0.77*** | 0.27 | 0.47** | 0.49*** |
| **S** | | | | | | | -0.73*** | -0.82*** | -0.73*** |
| **Si** | | | | | | | | 0.80*** | 0.58*** |
| **ASI** | | | | | | | | | 0.83*** |
| **Minerals** | | | | | | | | | |

**TAC (upper 0–50cm)**

*** p < 0.001; ** p < 0.01; * p < 0.05

https://doi.org/10.5194/egusphere-2025-400
Preprint. Discussion started: 19 February 2025


## Appendix F: Historical hurricanes

**Table F1. List of hurricanes that passed within 100 km or closer to the Magdalen Islands, Québec, with recorded wind of the hurricane at that time and whether or not there were known impacts.**

| # | Date | Hurricane | Wind speed (km/h) | Known impacts | Listed in |
|---|---|---|---|---|---|
| 1 | 2019-09-07 | Dorian | 139 | Yes (Avila et al., 2020) | IBTrACTS |
| 2 | 2014-07-06 | Arthur | 83 | No | IBTrACTS |
| 3 | 2010-09-04 | Earl | 101 | No | IBTrACTS |
| 4 | 2001-10-15 | Karen | 74 | No | IBTrACTS |
| 5 | 1999-09-18 | Floyd | 65 | No | IBTrACTS |
| 6 | 1996-10-10 | Josephine | 83 | No | IBTrACTS |
| 7 | 1996-07-14 | Bertha | 93 | No | IBTrACTS |
| 8 | 1988-08-08 | Alberto | 65 | No | IBTrACTS |
| 9 | 1979-09-07 | David | 93 | No | IBTrACTS |
| 10 | 1975-07-28 | Blanche | 111 | Yes (Le Droit, July 29 1975; Le Soleil, July 29 1975 ) | IBTrACTS |
| 11 | 1962-07-04 | Not named | 65 | No | IBTrACTS |
| 12 | 1959-07-12 | Cindy | 65 | No | IBTrACTS |
| 13 | 1950-08-21 | Able | 74 | No | IBTrACTS |
| 14 | 1944-09-15 | Not named | 83 | No | IBTrACTS |
| 15 | 1940-09-17 | Not named | 111 | No | IBTrACTS |
| 16 | 1937-09-26 | Not named | 111 | No | IBTrACTS |
| 17 | 1936-09-25 | Not named | 102 | No | IBTrACTS |
| 18 | 1934-09-10 | Not named | 46 | No | IBTrACTS |
| 19 | 1934-06-21 | Not named | 74 | No | IBTrACTS |
| 20 | 1933-10-30 | Not named | 93 | No | IBTrACTS |
| 21 | 1933-09-18 | Not named | 111 | No | IBTrACTS |
| 22 | 1927-08-25 | 1927 August Gale† | 157 | Yes (Landry, 1989, 1994) | IBTrACTS |
| 23 | 1924-08-27 | Not named | 111 | No | IBTrACTS |
| 24 | 1917-08-11 | Not named | 83 | No | IBTrACTS |
| 25 | 1900-09-13 | The Galveston Hurricane† | 120 | Yes (Landry, 1989, 1994) | IBTrACTS |
| 26 | 1899-11-02 | Not named | 74 | No | IBTrACTS |
| 27 | 1898-10-06 | Not named | 46 | No | IBTrACTS |
| 28 | 1896-10-15 | Not named | 65 | No | IBTrACTS |
| 29 | 1891-10-15 | Not named | 65 | No | IBTrACTS |
| 30 | 1889-10-08 | Not named | 74 | No | IBTrACTS |
| 31 | 1888-08-23 | Not named | 93 | No | IBTrACTS |

https://doi.org/10.5194/egusphere-2025-400
Preprint. Discussion started: 19 February 2025


| | | | | | |
|---|---|---|---|---|---|
| 32 | 1879-11-21 | Not named | 120 | Yes (Landry, 1989, 1994) | IBTrACTS |
| 33 | 1879-08-20 | Not named | 111 | No | IBTrACTS |
| 34 | 1877-11-30 | Not named | 74 | No | IBTrACTS |
| 35 | 1875-10-16 | Not named | 74 | No | IBTrACTS |
| 36 | 1873-08-25 | 1873 Great August Gale†‡ | 160 | Yes (Landry, 1989, 1994) | Shipwreck record(Landry, 1989, 1994) |
| 37 | 1871-10-13 | Not named | 111 | No | IBTrACTS |
| 38 | 1860-08-27 | Not named | 65 | No | IBTrACTS |
| 39 | 1851-10-14 | Not named | 56 | No | IBTrACTS |

**† Non-official but common names found in the literature to describe these events. ‡ The 1873 Great August Gale passed approximately 500 km south of the Magdalen Islands, near Sable Island in the North Atlantic Ocean. Nevertheless, it still was one of the most destructive storms in the Magdalen Islands and is well-documented.**

https://doi.org/10.5194/egusphere-2025-400
Preprint. Discussion started: 19 February 2025


## References

Adomat, F. and Gischler, E.: Assessing the suitability of Holocene environments along the central Belize coast, Central America, for the reconstruction of hurricane records, Int. J. Earth Sci., 106, 283-309, https://doi.org/10.1007/s00531-016-1319-y, 2017.

Aitchison, J.: The statistical analysis of compositional data, J. Roy. Stat. Soc. B. Met., 44, 139-160, https://doi.org/10.1111/j.2517-6161.1982.tb01195.x, 1982.

Aquino-López, M. A., Blaauw, M., Christen, J. A., and Sanderson, N. K.: Bayesian Analysis of 210-Pb Dating, 23, 317-333, 2018.

Avila, L.: National hurricane center tropical cyclone report - Hurricane Juan, NOAA National Hurricane Center, 11pp., 2003.

Avila, L., Stewart, S., Berg, R., and Hagen, A.: National hurricane center tropical cyclone report - Hurricane Dorian, NOAA National Hurricane Center, 74pp., 2020.

Baker, A. J., Hodges, K. I., Schiemann, R. K., and Vidale, P. L.: Historical variability and lifecycles of North Atlantic midlatitude cyclones originating in the tropics, J. Geophys. Res.-Atmos., 126, e2020JD033924, https://doi.org/10.1029/2020JD033924, 2021.

Barnett, R., Bernatchez, P., Garneau, M., and Juneau, M. N.: Reconstructing late Holocene relative sea-level changes at the Magdalen Islands (Gulf of St. Lawrence, Canada) using multi-proxy analyses, J. Quaternary Sci., 32, 380-395, https://doi.org/10.1002/jqs.2931, 2017.

Barnett, R., Bernatchez, P., Garneau, M., Brain, M., Charman, D., Stephenson, D., Haley, S., and Sanderson, N.: Late Holocene sea-level changes in eastern Québec and potential drivers, Quaternary Sci. Rev., 203, 151-169, https://doi.org/10.1016/j.quascirev.2018.10.039, 2019.

Bengtsson, L. and Enell, M.: Chemical analysis, in: Handbook of Holocene Palaeoecology and Palaeohydrology, edited by: Berglund BE, Wiley Interscience, John Wiley & Sons Ltd., Chichester, https://doi.org/10.1002/jqs.3390010111, 1986.

Bernatchez, P., Boucher-Brossard, G., and Sigouin-Cantin, M.: Contribution des archives à l'étude des événements météorologiques et géomorphologiques causant des dommages aux côtes du Québec maritime et analyse des tendances, des fréquences et des temps de retour des conditions météo-marines extrêmes, Chaire de recherche en géoscience côtière, Laboratoire de dynamique et de gestion intégrée des zones côtières, Université du Québec à Rimouski, 140pp., 2012.

Bertrand, S., Tjallingii, R., Kylander, M. E., Wilhelm, B., Roberts, S. J., Arnaud, F., Brown, E., and Bindler, R.: Inorganic geochemistry of lake sediments: A review of analytical techniques and guidelines for data interpretation, Eart-Sci. Rev., 104639, https://doi.org/10.1016/j.earscirev.2023.104639, 2023.

Besonen, M. R., Bradley, R. S., Mudelsee, M., Abbott, M. B., and Francus, P.: A 1,000-year, annually-resolved record of hurricane activity from Boston, Massachusetts, Geophys. Res. Lett., 35, https://doi.org/10.1029/2008GL033950, 2008.

Bibliothèque et Archive Nationale du Québec: BAnQ archive numérique, https://numerique.banq.qc.ca/, last access: 2024.

Björckl, S. and Clemmensen, L. B.: Aeolian sediment in raised bog deposits, Halland, SW Sweden: a new proxy record of Holocene winter storminess variation in southern Scandinavia?, Holocene, 14, 677-688, https://doi.org/10.1191/0959683604hl746rp, 2004.

Blaauw, M., Christen, J., and Aquino-Lopez, M.: rplum: Bayesian Age-Depth Modelling of Cores Dated by Pb-210 (R package version 0.5.1), CRAN [code], http://doi.org/10.32614/CRAN.package.rplum, 2024.

Boldt, K. V., Lane, P., Woodruff, J. D., and Donnelly, J. P.: Calibrating a sedimentary record of overwash from Southeastern New England using modeled historic hurricane surges, Mar. Geol., 275, 127-139, https://doi.org/10.1016/j.margeo.2010.05.002, 2010.

https://doi.org/10.5194/egusphere-2025-400
Preprint. Discussion started: 19 February 2025


Brandon, C. M., Woodruff, J. D., Lane, D. P., and Donnelly, J. P.: Tropical cyclone wind speed constraints from resultant storm surge deposition: A 2500 year reconstruction of hurricane activity from St. Marks, FL, Geochem. Geophy. Geosy., 14, 2993-3008, https://doi.org/10.1002/ggge.20217, 2013.

Braun, E., Meyer, B., Deocampo, D., and Kiage, L. M.: A 3000 yr paleostorm record from St. Catherines Island, Georgia, Estuar., Coast., Shelf S., 196, 360-372, https://doi.org/10.1016/j.ecss.2017.05.021, 2017.

Bregy, J. C., Wallace, D. J., Minzoni, R. T., and Cruz, V. J.: 2500-year paleotempestological record of intense storms for the northern Gulf of Mexico, United States, Mar. Geol., 396, 26-42, https://doi.org/10.1016/j.margeo.2017.09.009, 2018.

Bregy, J. C., Maxwell, J. T., Robeson, S. M., Harley, G. L., Elliott, E. A., and Heeter, K. J.: US Gulf Coast tropical cyclone precipitation influenced by volcanism and the North Atlantic subtropical high, Commun. Earth Environ., 3, 164, https://doi.org/10.1038/s43247-022-00494-7, 2022.

Brisebois, D.: Lithostratigraphie des strates permo-carboniferes, de l'archipel des Iles de la Madeleine, Direction générale des énergies conventionnelles, DPV-796, 48pp., 1981.

Canadian Ice Service: Seasonal Summary, Eastern Canada, Winter 2021-2022, Environment and Climate Change Canada, 29pp., 2022.

Chartrand, P. G., Sonnentag, O., Sanderson, N. K., and Garneau, M.: Recent peat and carbon accumulation on changing permafrost landforms along the Mackenzie River valley, Northwest Territories, Canada, Environ. Res. Lett., 18, 095002, https://doi.org/10.1088/1748-9326/ace9ed, 2023.

Chiang, J. C. H. and Vimont, D. J.: Analogous Pacific and Atlantic Meridional Modes of Tropical Atmosphere–Ocean Variability, J. Climate, 17, 4143-4158, https://doi.org/10.1175/JCLI4953.1, 2004.

Colbert, A. J. and Soden, B. J.: Climatological Variations in North Atlantic Tropical Cyclone Tracks, J. Climate, 25, 657-673, https://doi.org/10.1175/JCLI-D-11-00034.1, 2012.

Crann, C. A., Murseli, S., St-Jean, G., Zhao, X., Clark, I. D., and Kieser, W. E.: First status report on radiocarbon sample preparation techniques at the AE Lalonde AMS Laboratory (Ottawa, Canada), Radiocarbon, 59, 695-704, https://doi.org/10.1017/RDC.2016.55, 2017.

Croudace, I. W. and Rothwell, R. G.: Micro-XRF Studies of Sediment Cores: Applications of a non-destructive tool for the environmental sciences, Developments in Paleoenvironmental Research, 17, Springer, Dordrecht, Netherlands, 656 pp., https://doi.org/10.1007/978-94-017-9849-5, 2015.

De Vleeschouwer, F., Sikorski, J., and Fagel, N.: Development of lead-210 measurement in peat using polonium extraction. A procedural comparison, Geochronometria, 36, 1-8, https://doi.org/10.2478/v10003-010-0013-5, 2010.

Dean, W. E.: Determination of carbonate and organic matter in calcareous sediments and sedimentary rocks by loss on ignition; comparison with other methods, J. Sediment Res., 44, 242-248, https://doi.org/10.1306/74D729D2-2B21-11D7-8648000102C1865D, 1974.

Denommee, K., Bentley, S., and Droxler, A.: Climatic controls on hurricane patterns: a 1200-y near-annual record from Lighthouse Reef, Belize, Sci. Rep., 4, 3876, https://doi.org/10.1038/srep03876, 2014.

Derksen, C., Burgess, D., Duguay, C., Howell, S., Mudryk, L., Smith, S., Thackeray, C., and Kirchmeier-Young, M.: Changes in snow, ice, and permafrost across Canada, in: Canada's changing climate report, edited by: Bush, E., and Lemmen, D. S., Government of Canada, 194-260, https://doi.org/10.4095/308279, 2019.

Dickie, J. and Wach, G.: A major midlatitude hurricane in the Little Ice Age, Clim. Past., 20, 1141-1160, https://doi.org/10.5194/cp-20-1141-2024, 2024.

Donnelly, J. P., Hawkes, A. D., Lane, P., MacDonald, D., Shuman, B. N., Toomey, M. R., van Hengstum, P. J., and Woodruff, J. D.: Climate forcing of unprecedented intense-hurricane activity in the last 2000 years, Earth's Future, 3, 49-65, https://doi.org/10.1002/2014EF000274, 2015.

https://doi.org/10.5194/egusphere-2025-400
Preprint. Discussion started: 19 February 2025


Dredge, L. A., Mott, R. J., and Grant, D. R.: Quaternary stratigraphy, paleoecology, and glacial geology, Îles de la Madeleine, Quebec, Can. J. Earth Sci., 29, 1981-1996, https://doi.org/10.1139/e92-154, 1992.

Environment and Climate Change Canada: Canadian Climate Normals 1981-2010 Station Data - ILES DE LA MADELEINE A, https://climate.weather.gc.ca/climate_normals/results_1981_2010_e.html?stnID=5748&autofwd=1, last access: 30 July 2024.

Forbes, D. L., Parkes, G. S., Manson, G. K., and Ketch, L. A.: Storms and shoreline retreat in the southern Gulf of St. Lawrence, Mar. Geol., 210, 169-204, https://doi.org/10.1016/j.margeo.2004.05.009, 2004.

Fortin, J.-C. and Larocque, P.: Histoire des Iles-de-la-Madeleine, Institut quebecois de recherche sur la culture, Les Éditions de l'IQRC et Les Presses de l'Université Laval, Sainte-Foy, 400 pp., https://doi.org/10.7202/014675ar, 2003.

Gahtan, J., K. R. Knapp, C. J. Schreck, H. J. Diamond, J. P. Kossin, and Kruk, M. C.: International Best Track Archive for Climate Stewardship (IBTrACS) Project (Version 4r01) [North Atlantic Ocean], NOAA National Centers for Environmental Information [dataset], https://doi.org/10.25921/82ty-9e16, 2024.

Garneau, M.: Collection de référence de graines et autres macrofossiles végétaux de taxons provenant du Québec méridional et boréal et de l'arctique canadien, Geol. Surv. of Can., Ottawa, Ont., Dossier publique 3048, 38 pp. , 1995.

Goslin, J., Gałka, M., Sander, L., Fruergaard, M., Mokenbusch, J., Thibault, N., and Clemmensen, L. B.: Decadal variability of north-eastern Atlantic storminess at the mid-Holocene: New inferences from a record of wind-blown sand, western Denmark, Global Planet. Change, 180, 16-32, https://doi.org/10.1016/j.gloplacha.2019.05.010, 2019.

Heiri, O., Lotter, A. F., and Lemcke, G.: Loss on ignition as a method for estimating organic and carbonate content in sediments: reproducibility and comparability of results, J. Paleolimnol, 25, 101-110, https://doi.org/10.1023/A:1008119611481, 2001.

Hétu, B., Rémillard, A. M., Bernatchez, P., and St-Onge, G.: Landforms and Landscapes of the Magdalen Islands: The Role of Geology and Climate, in: Landscapes and Landforms of Eastern Canada. World Geomorphological Landscapes, edited by: Slaymaker, O., and Catto, N., Springer, Cham, 431-451, https://doi.org/10.1007/978-3-030-35137-3_19, 2020.

Hewett, D.: Menyanthes trifoliata L, J. Ecol., 52, 723-735, https://doi.org/10.2307/2257858, 1964.

Huang, B., Thorne, P. W., Banzon, V. F., Boyer, T., Chepurin, G., Lawrimore, J. H., Menne, M. J., Smith, T. M., Vose, R. S., and Zhang, H.-M.: Extended Reconstructed Sea Surface Temperature, Version 5 (ERSSTv5): Upgrades, Validations, and Intercomparisons, J. Climate, 30, 8179-8205, https://doi.org/10.1175/JCLI-D-16-0836.1, 2017.

Hundecha, Y., St-Hilaire, A., Ouarda, T., El Adlouni, S., and Gachon, P.: A nonstationary extreme value analysis for the assessment of changes in extreme annual wind speed over the Gulf of St. Lawrence, Canada, J. Appl. Meteorol. Clim., 47, 2745-2759, https://doi.org/10.1175/2008JAMC1665.1, 2008.

Husson, F., Josse, J., Le, S., and Mazet, J.: FactoMineR: Multivariate Exploratory Data Analysis and Data Mining (R package version 2.11), CRAN [code], http://doi.org/10.32614/CRAN.package.FactoMineR, 2024.

Insurance Bureau of Canada: Hurricane Fiona causes $660 million in insured damage, http://www.ibc.ca/ns/resources/media-centre/media-releases/hurricane-fiona-causes-660-million-in-insured-damage, last access: 31 October 2022.

Irish, J. L., Resio, D. T., and Ratcliff, J. J.: The influence of storm size on hurricane surge, J. Phys. Oceangraph. , 38, 2003-2013, https://doi.org/10.1175/2008JPO3727.1, 2008.

Jardine, D. E., Wang, X., and Fenech, A. L.: Highwater mark collection after post tropical storm Dorian and implications for Prince Edward Island, Canada, Water, 13, 3201, https://doi.org/10.3390/w13223201, 2021.

Juggins, S.: rioja: Analyss of Quaternary Science Data (R package version 1.0-7), CRAN [code], http://doi.org/10.32614/CRAN.package.rioja, 2024.

Kern, O. A., Koutsodendris, A., Maechtle, B., Christanis, K., Schukraft, G., Scholz, C., Kotthoff, U., and Pross, J.: XRF core scanning yields reliable semiquantitative data on the elemental composition of highly organic-rich sediments: Evidence from

the Füramoos peat bog (Southern Germany), Sci. Total Environ., 697, 134110, https://doi.org/10.1016/j.scitotenv.2019.134110, 2019.

Klotzbach, P. J. and Gray, W. M.: Multidecadal variability in North Atlantic tropical cyclone activity, J. Climate, 21, 3929-3935, https://doi.org/10.1175/2008JCLI2162.1, 2008.

Knapp, K. R., Kruk, M. C., Levinson, D. H., Diamond, H. J., and Neumann, C. J.: The international best track archive for climate stewardship (IBTrACS) unifying tropical cyclone data, B. Am. Meteorol. Soc., 91, 363-376, https://doi.org/10.1175/2009BAMS2755.1, 2010.

Kossin, J. P.: Hurricane intensification along United States coast suppressed during active hurricane periods, Nature, 541, 390-393, https://doi.org/10.1038/nature20783, 2017.

Kossin, J. P. and Vimont, D. J.: A more general framework for understanding Atlantic hurricane variability and trends, B. Am. Meteorol. Soc., 88, 1767-1782, https://doi.org/10.1175/BAMS-88-11-1767, 2007.

Kossin, J. P., Camargo, S. J., and Sitkowski, M.: Climate modulation of North Atlantic hurricane tracks, J. Climate, 23, 3057-3076, https://doi.org/10.1175/2010JCLI3497.1, 2010.

Kuhry, P. and Turunen, J.: The postglacial development of boreal and subarctic peatlands, in: Boreal peatland ecosystems. Ecological Studies, vol. 188, edited by: Wieder, R. K., and Vitt, D. H., Springer, Berlin, Heidelberg, Germany, 25-46, https://doi.org/10.1007/978-3-540-31913-9_3, 2006.

Kylander, M. E., Söderlindh, J., Schenk, F., Gyllencreutz, R., Rydberg, J., Bindler, R., Martínez Cortizas, A., and Skelton, A.: It's in your glass: a history of sea level and storminess from the Laphroaig bog, Islay (southwestern Scotland), Boreas, 49, 152-167, https://doi.org/10.1111/bor.12409, 2020.

Kylander, M. E., Martínez-Cortizas, A., Sjöström, J. K., Gåling, J., Gyllencreutz, R., Bindler, R., Alexanderson, H., Schenk, F., Reinardy, B. T., and Chandler, B. M.: Storm chasing: Tracking Holocene storminess in southern Sweden using mineral proxies from inland and coastal peat bogs, Quaternary Sci. Rev., 299, 107854, https://doi.org/10.1016/j.quascirev.2022.107854, 2023.

Landry, F.: Derniere Course: Aventures maritimes dans le Golfe du Saint-Laurent, La Boussole, Havre-Aubert, Ile-de-la-Madeleine, 1989.

Landry, F.: Piege de sable, La Boussole, Havre-Aubert, Iles-de-la-Madeleine, 1994.

Lane, P., Donnelly, J. P., Woodruff, J. D., and Hawkes, A. D.: A decadally-resolved paleohurricane record archived in the late Holocene sediments of a Florida sinkhole, Mar. Geol., 287, 14-30, https://doi.org/10.1016/j.margeo.2011.07.001, 2011.

Lapointe, F., Bradley, R. S., Francus, P., Balascio, N. L., Abbott, M. B., Stoner, J. S., St-Onge, G., De Coninck, A., and Labarre, T.: Annually resolved Atlantic sea surface temperature variability over the past 2,900 y, P. Natl. Acad. Sci. USA, 117, 27171-27178, https://doi.org/10.1073/pnas.2014166117, 2020.

Le Droit: Blanche a arraché de nombreux toits aux Iles-de-la-Madeleine, July 29 1975.

Le Soleil: Blanche isole les Iles-de-la-Madeleine du continent, 1, July 29 1975

Liu, D., Bertrand, S., and Weltje, G. J.: An empirical method to predict sediment grain size from inorganic geochemical measurements, Geochem. Geophy. Geosy., 20, 3690-3704, https://doi.org/10.1029/2018GC008154, 2019.

Liu, K.-b. and Fearn, M. L.: Lake-sediment record of late Holocene hurricane activities from coastal Alabama, Geology, 21, 793-796, https://doi.org/10.1130/0091-7613(1993)021<0793:LSROLH>2.3.CO;2, 1993.

Liu, K.-b. and Fearn, M. L.: Reconstruction of prehistoric landfall frequencies of catastrophic hurricanes in northwestern Florida from lake sediment records, Quaternary Res., 54, 238-245, https://doi.org/10.1006/qres.2000.2166, 2000.

Longman, J., Veres, D., and Wennrich, V.: Utilisation of XRF core scanning on peat and other highly organic sediments, Quatern. Int., 514, 85-96, https://doi.org/10.1016/j.quaint.2018.10.015, 2019.

https://doi.org/10.5194/egusphere-2025-400
Preprint. Discussion started: 19 February 2025


Magnan, G. and Garneau, M.: Evaluating long-term regional climate variability in the maritime region of the St. Lawrence North Shore (eastern Canada) using a multi-site comparison of peat-based paleohydrological records, J. Quaternary Sci., 29, 209-220, https://doi.org/10.1002/jqs.2694, 2014.

Magnan, G., Garneau, M., and Payette, S.: Holocene development of maritime ombrotrophic peatlands of the St. Lawrence North Shore in eastern Canada, Quaternary Res., 82, 96-106, https://doi.org/10.1016/j.yqres.2014.04.016, 2014.

Mann, M. E., Woodruff, J. D., Donnelly, J. P., and Zhang, Z.: Atlantic hurricanes and climate over the past 1,500 years, Nature, 460, 880-883, https://doi.org/10.1038/nature08219, 2009a.

Mann, M. E., Zhang, Z., Rutherford, S., Bradley, R. S., Hughes, M. K., Shindell, D., Ammann, C., Faluvegi, G., and Ni, F.: Global signatures and dynamical origins of the Little Ice Age and Medieval Climate Anomaly, Science, 326, 1256-1260, http://doi.org/10.1126/science.1177303, 2009b.

Ministère de l'Environnement et de la Lutte contre les changements climatiques: Habitat floristique de la Tourbière-du-Lac-Maucôque, https://www.environnement.gouv.qc.ca/biodiversite/habitats/tourbiere-lac-maucoque/index.htm, last access: 27 May 2021

Ministère de l'Environnement et de la Lutte contre les changements climatiques: Habitat floristique de la Tourbière-de-L'Anse-à-la-Cabane, https://www.environnement.gouv.qc.ca/biodiversite/habitats/tourbiere-anse-cabane/index.htm, last access: 27 May 2021.

Monica, S. B., Wallace, D. J., Wallace, E. J., Du, X., Dee, S. G., and Anderson, J. B.: 4500-year paleohurricane record from the Western Gulf of Mexico, Coastal Central TX, USA, Mar. Geol., 473, 107303, https://doi.org/10.1016/j.margeo.2024.107303, 2024.

Oliva, F., Peros, M., and Viau, A.: A review of the spatial distribution of and analytical techniques used in paleotempestological studies in the western North Atlantic Basin, Prog. Phys. Geog., 41, 171-190, https://doi.org/10.1177/0309133316683899, 2017.

Oliva, F., Peros, M., Viau, A., Reinhardt, E., Nixon, F., and Morin, A.: A multi-proxy reconstruction of tropical cyclone variability during the past 800 years from Robinson Lake, Nova Scotia, Canada, Mar. Geol., 406, 84-97, https://doi.org/10.1016/j.margeo.2018.09.012, 2018.

Pasch, R. J., Penny, A. B., and Berg, R.: National hurricane center tropical cyclone report - Hurricane Fiona, NOAA National Hurricane Center, 2023.

Patterson, R. T., Nasser, N. A., Reinhardt, E. G., Patterson, C. W., Gregory, B. R., Mazzella, V., Roe, H. M., and Galloway, J. M.: End-Member Mixing Analysis as a Tool for the Detection of Major Storms in Lake Sediment Records, Paleoceanogr. Paleoclimatol., 37, e2022PA004510, https://doi.org/10.1029/2022PA004510, 2022.

Peros, M., Chan, K., Magnan, G., Ponsford, L., Carroll, J., and McCloskey, T.: A 9600-year record of water table depth, vegetation and fire inferred from a raised peat bog, Prince Edward Island, Canadian Maritimes, J. Quaternary Sci., 31, 512-525, http://doi.org/10.1002/jqs.2875, 2016.

Perrier, L., Garneau, M., Pratte, S., and Sanderson, N. K.: Climate-driven Holocene ecohydrological and carbon dynamics from maritime peatlands of the Gulf of St. Lawrence, eastern Canada, 09596836221095978, 2022.

Plante, M., Son, S. W., Atallah, E., Gyakum, J., and Grise, K.: Extratropical cyclone climatology across eastern Canada, Int. J. Climatol., 35, 2759-2776, https://doi.org/10.1002/joc.4170, 2015.

Pleskot, K., Cwynar, L. C., Kowalczyk, C., Kokociński, M., and Szczuciński, W.: Refining the history of extreme coastal events in southern Newfoundland, NW Atlantic, with lake sediment archives, Quaternary Sci. Rev., 322, 108401, https://doi.org/10.1016/j.quascirev.2023.108401, 2023.

Prest, V., Terasme, J., Matthews, J., JV, and Lichti-Federovich, S.: Late-Quaternary History of Magdalen Islands, Quebec, Atlantic Geol., 12, 39-60, https://doi.org/10.4138/1835, 1976.

https://doi.org/10.5194/egusphere-2025-400
Preprint. Discussion started: 19 February 2025


Public Safety Canada: Canadian Disaster Database, https://bdc.securitepublique.gc.ca/prnt-eng.aspx?cultureCode=en-Ca&eventTypes=%27HU%27&normalizedCostYear=1, last access: 29 July 2024.

Pye, K. and Tsoar, H.: Aeolian Sand and Sand Dunes, Springer Berlin, Heidelberg, 458 pp., https://doi.org/10.1007/978-3-540-85910-9, 2008.

Reimer, P. J., Austin, W. E. N., Bard, E., Bayliss, A., Blackwell, P. G., Bronk Ramsey, C., Butzin, M., Cheng, H., Edwards, R. L., Friedrich, M., Grootes, P. M., Guilderson, T. P., Hajdas, I., Heaton, T. J., Hogg, A. G., Hughen, K. A., Kromer, B., Manning, S. W., Muscheler, R., Palmer, J. G., Pearson, C., van der Plicht, J., Reimer, R. W., Richards, D. A., Scott, E. M., Southon, J. R., Turney, C. S. M., Wacker, L., Adolphi, F., Büntgen, U., Capano, M., Fahrni, S. M., Fogtmann-Schulz, A., Friedrich, R., Köhler, P., Kudsk, S., Miyake, F., Olsen, J., Reinig, F., Sakamoto, M., Sookdeo, A., and Talamo, S.: The IntCal20 Northern Hemisphere Radiocarbon Age Calibration Curve (0–55 cal kBP), Radiocarbon, 62, 725-757, https://doi.org/10.1017/RDC.2020.41, 2020.

Rémillard, A. M., Buylaert, J.-P., Murray, A., St-Onge, G., Bernatchez, P., and Hétu, B.: Quartz OSL dating of late Holocene beach ridges from the Magdalen Islands (Quebec, Canada), Quat. Geochronol., 30, 264-269, https://doi.org/10.1016/j.quageo.2015.03.013, 2015.

Rémillard, A. M., St-Onge, G., Bernatchez, P., Hétu, B., Buylaert, J.-P., Murray, A. S., and Lajeunesse, P.: Relative sea-level changes and glacio-isostatic adjustment on the Magdalen Islands archipelago (Atlantic Canada) from MIS 5 to the late Holocene, Quaternary Sci. Rev., 171, 216-233, https://doi.org/10.1016/j.quascirev.2017.07.015, 2017.

Rémillard, A. M., St-Onge, G., Bernatchez, P., Hétu, B., Buylaert, J. P., Murray, A. S., and Vigneault, B.: Chronology and stratigraphy of the Magdalen Islands archipelago from the last glaciation to the early Holocene: new insights into the glacial and sea-level history of eastern Canada, Boreas, 45, 604-628, https://doi.org/10.1111/bor.12179, 2016.

Rodysill, J. R., Donnelly, J. P., Sullivan, R., Lane, P. D., Toomey, M., Woodruff, J. D., Hawkes, A. D., MacDonald, D., d'Entremont, N., and McKeon, K.: Historically unprecedented Northern Gulf of Mexico hurricane activity from 650 to 1250 CE, Sci. Rep., 10, 1-17, https://doi.org/10.1038/s41598-020-75874-0, 2020.

Sabina, A. P.: Rocks and minerals for the collector: Iles de la Madeleine, Quebec, the Island of Newfoundland, and Labrador, Geol. Surv. of Can., Ottawa, Ont., Miscellaneous Report 58, https://doi.org/10.4095/214397, 2003.

Shotyk, W.: Review of the inorganic geochemistry of peats and peatland waters, Earth-Sci. Rev., 25, 95-176, https://doi.org/10.1016/0012-8252(88)90067-0, 1988.

Sjöström, J. K., Cortizas, A. M., Hansson, S. V., Sánchez, N. S., Bindler, R., Rydberg, J., Mörth, C.-M., Ryberg, E. E., and Kylander, M. E.: Paleodust deposition and peat accumulation rates–Bog size matters, Chem. Geol., 554, 119795, https://doi.org/10.1016/j.chemgeo.2020.119795, 2020.

Sjöström, J. K., Gyllencreutz, R., Cortizas, A. M., Nylund, A., Piilo, S. R., Schenk, F., McKeown, M., Ryberg, E. E., and Kylander, M. E.: Holocene storminess dynamics in northwestern Ireland: Shifts in storm duration and frequency between the mid-and late Holocene, Quaternary Sci. Rev., 337, 108803, https://doi.org/10.1016/j.quascirev.2024.108803, 2024.

ten Brink, U. S., Chaytor, J., Geist, E. L., Brothers, D. S., and Andrews, B. D.: Assessment of tsunami hazard to the US Atlantic margin, Mar. Geol., 353, 31-54, https://doi.org/10.1016/j.margeo.2014.02.011, 2014.

Ting, M., Kossin, J. P., Camargo, S. J., and Li, C.: Past and future hurricane intensity change along the US east coast, Sci. Rep., 9, 1-8, https://doi.org/10.1038/s41598-019-44252-w, 2019.

Troels-Smith, J.: Karakterisering af lose jordater (Characterization of unconsolidated sediments), Danmarks Geologiske Undersogelse IV. Række, 3, 1-73, https://doi.org/10.34194/raekke4.v3.6989, 1955.

Vaasma, T.: Grain-size analysis of lacustrine sediments: a comparison of pre-treatment methods, Estonian J. Ecol., 57, https://doi.org/10.3176/eco.2008.4.01, 2008.

https://doi.org/10.5194/egusphere-2025-400
Preprint. Discussion started: 19 February 2025


Vacchi, M., Engelhart, S. E., Nikitina, D., Ashe, E. L., Peltier, W. R., Roy, K., Kopp, R. E., and Horton, B. P.: Postglacial relative sea-level histories along the eastern Canadian coastline, Quaternary Sci. Rev., 201, 124-146, https://doi.org/10.1016/j.quascirev.2018.09.043, 2018.

van de Plassche, O., Erkens, G., van Vliet, F., Brandsma, J., van der Borg, K., and de Jong, A. F.: Salt-marsh erosion associated with hurricane landfall in southern New England in the fifteenth and seventeenth centuries, Geology, 34, 829-832, https://doi.org/10.1130/G22598.1, 2006.

Van den Boogaart, K. G. and Tolosana-Delgado, R.: "Compositions": a unified R package to analyze compositional data, Comput. Geosci., 34, 320-338, https://doi.org/10.1016/j.cageo.2006.11.017, 2008.

Van den Boogaart, K. G. and Tolosana-Delgado, R.: Analyzing compositional data with R, in: Use R!, edited by: Gentleman, R., Hornik, K., and Parmigiani, G. G., Springer, 258, https://doi.org/10.1007/978-3-642-36809-7, 2013.

Van den Boogaart, K. G., Tolosana-Delgado, R., and Bren, M.: compositions: Compositional Data Analysis (R package version 2.0-8), CRAN [code], 10.32614/CRAN.package.compositions, 2024.

van Geel, B., Buurman, J., and Waterbolk, H. T.: Archaeological and palaeoecological indications of an abrupt climate change in The Netherlands, and evidence for climatological teleconnections around 2650 BP, J. Quaternary Sci., 11, 451-460, https://doi.org/10.1002/(SICI)1099-1417(199611/12)11:6<451::AID-JQS275>3.0.CO;2-9, 1996.

van Geel, B., Heijnis, H., Charman, D. J., Thompson, G., and Engels, S.: Bog burst in the eastern Netherlands triggered by the 2.8 kyr BP climate event, Holocene, 24, 1465-1477, https://doi.org/10.1177/0959683614544066, 2014.

van Hengstum, P. J., Donnelly, J. P., Toomey, M. R., Albury, N. A., Lane, P., and Kakuk, B.: Heightened hurricane activity on the Little Bahama Bank from 1350 to 1650 AD, Cont. Shelf Res., 86, 103-115, https://doi.org/10.1016/j.csr.2013.04.032, 2014.

Vandel, E., Vaasma, T., Sugita, S., Tõnisson, H., Jaagus, J., Vilumaa, K., Anderson, A., and Kont, A.: Reconstruction of past storminess: Evaluation of an indicator approach using aeolian mineral grains buried in peat deposits, Estonia, Quaternary Sci. Rev., 218, 215-227, https://doi.org/10.1016/j.quascirev.2019.06.026, 2019.

Verhaegen, J., Weltje, G., and Munsterman, D.: Workflow for analysis of compositional data in sedimentary petrology: provenance changes in sedimentary basins from spatio-temporal variation in heavy-mineral assemblages, Geol. Mag., 156, 1111-1130, https://doi.org/10.1017/S0016756818000584, 2019.

Vimont, D. J. and Kossin, J. P.: The Atlantic meridional mode and hurricane activity, Geophys. Res. Lett., 34, https://doi.org/10.1029/2007GL029683, 2007.

Wallace, E., Donnelly, J. P., van Hengstum, P. J., Wiman, C., Sullivan, R., Winkler, T., d'Entremont, N., Toomey, M., and Albury, N.: Intense hurricane activity over the past 1500 years at South Andros Island, The Bahamas, Paleoceanogr. Paleoclimatol., 34, 1761-1783, https://doi.org/10.1029/2019PA003665, 2019.

Wallace, E., Donnelly, J., van Hengstum, P., Winkler, T., Dizon, C., LaBella, A., Lopez, I., d'Entremont, N., Sullivan, R., and Woodruff, J.: Regional shifts in paleohurricane activity over the last 1500 years derived from blue hole sediments offshore of Middle Caicos Island, Quaternary Sci. Rev., 268, 107126, https://doi.org/10.1016/j.quascirev.2021.107126, 2021a.

Wallace, E., Donnelly, J., van Hengstum, P., Winkler, T., McKeon, K., MacDonald, D., d'Entremont, N., Sullivan, R., Woodruff, J., and Hawkes, A.: 1,050 years of hurricane strikes on Long Island in The Bahamas, Paleoceanogr. Paleoclimatol., 36, e2020PA004156, https://doi.org/10.1029/2020PA004156, 2021b.

Wang, J., Yang, B., Ljungqvist, F. C., Luterbacher, J., Osborn, T. J., Briffa, K. R., and Zorita, E.: Internal and external forcing of multidecadal Atlantic climate variability over the past 1,200 years, Nat. Geosci., 10, 512-517, https://doi.org/10.1038/ngeo2962, 2017.

Wang, Y., Jahan, S., Burnett, W. C., Wu, Z., Elsner, J. B., Means, G. H., Liu, J., and Jiang, S.: Late Holocene tropical cyclones linked to climatic and solar variability, Quaternary Sci. Rev., 334, 108710, https://doi.org/10.1016/j.quascirev.2024.108710, 2024.

https://doi.org/10.5194/egusphere-2025-400
Preprint. Discussion started: 19 February 2025


Weiss, D., Shotyk, W., Rieley, J., Page, S., Gloor, M., Reese, S., and Martinez-Cortizas, A.: The geochemistry of major and selected trace elements in a forested peat bog, Kalimantan, SE Asia, and its implications for past atmospheric dust deposition, Geochim. Cosmochim. Ac., 66, 2307-2323, https://doi.org/10.1016/S0016-7037(02)00834-7, 2002.

Wentworth, C. K.: A scale of grade and class terms for clastic sediments, J. Geol., 30, 377-392, https://doi.org/10.1086/622910, 1922.

Winkler, T., van Hengstum, P., Donnelly, J., Wallace, E., Albury, N., D'Entremont, N., Hawkes, A., Maio, C., Roberts, J., and Sullivan, R.: More frequent Hurricane passage across the Bahamian Archipelago during the little ice age, Paleoceanogr. Paleoclimatol., 38, e2023PA004623, https://doi.org/10.1029/2023PA004623, 2023.

Winkler, T. S., van Hengstum, P. J., Donnelly, J. P., Wallace, E. J., Sullivan, R. M., MacDonald, D., and Albury, N. A.: Revising evidence of hurricane strikes on Abaco Island (The Bahamas) over the last 700 years, Sci. Rep., 10, 16556, https://doi.org/10.1038/s41598-020-73132-x, 2020.

Wu, X., de Vernal, A., Fréchette, B., Moros, M., and Perner, K.: The signal of climate changes over the last two millennia in the Gulf of St. Lawrence, eastern Canada, Quaternary Res., 106, 28-43, https://doi.org/10.1017/qua.2021.56, 2022.

Yang, W., Wallace, E., Vecchi, G. A., Donnelly, J. P., Emile-Geay, J., Hakim, G. J., Horowitz, L. W., Sullivan, R. M., Tardif, R., and van Hengstum, P. J.: Last millennium hurricane activity linked to endogenous climate variability, Nat. Commun., 15, 816, https://doi.org/10.1038/s41467-024-45112, 2024.

Yang, Y., Maselli, V., Normandeau, A., Piper, D. J., Li, M. Z., Campbell, D. C., Gregory, T., and Gao, S.: Latitudinal response of storm activity to abrupt climate change during the last 6,500 years, Geophys. Res. Lett., 47, e2020GL089859, https://doi.org/10.1029/2020GL089859, 2020.